UCLouvain

École polytechnique de Louvain

Ultra-low-power instrumentation amplifiers with cuff electrodes for detection of epileptic seizures

Author: **Gabriel TINEM**
Supervisor: **David BOL**
Readers: **David BOL, Rémi DEKIMPE, Denis FLANDRE**
Academic year 2019–2020
Master [120] in Electrical Engineering

Abstract

While many advances have been done for identifying and processing data generated by epileptic seizures, there are still many challenges of how to deal with it without medicines. In order to detect these biosignals, some prerequisites must be respected, otherwise the whole sensing is degraded by noise or interferences. Not only the electrodes but also the amplification chain determines the quality of the observed signal that will be utilized in all processes.

This thesis discusses the types of electrodes used for ENG signals that could be extended to identifying epileptic seizures, alternatives for the core instrumentation amplifier with low-power consumption, configurations that make better use of all features presented and how to overcome non-idealities generated by the variable behaviour of the electrode-tissue interfaces. The source of the signals will be the vagus nerve, a complex but large nerve in the human body.

A key element in the whole process is how to deal with artefacts, since the order of magnitude from the captured useful ENG signals (μV) can be two or three orders of magnitude smaller than the one from muscles (EMG signals), not allowing proper measurements and analysis. For this, some configurations with the instrumentation amplifiers were analyzed checking advantages and drawbacks for each of them and the decision was made after the investigation of another non-ideality intrinsic from cuff electrodes: the impedance imbalances, that greatly degrades the property of linearized external potential interferences from the cuff electrodes. This issue was dealt by an addition of digital control over the gain from the amplifying chain that is possible in only one of these architectures.

Contents

Introduction

In recent times, more and more is known about epilepsy: a disease that affects many people worldwide. However, it is still very challenging to deal with it besides the use of medicines. Due to the need of new methods and techniques, many tests have been done in rats in order to detect ENG (electroneurogram) signals that might indicate physiological reactions due to some stimulus. For the human beings, the vagus nerve plays a very important role: it conveys information from the brain to other organs [28]. It is also the longest nerve of the autonomic nervous system and has influence on controlling the heart, lungs and digestive tract [1]. For this reason, VNS (vagus-nerve stimulation) showed up as an option for trying to attenuate and even avoid seizure effects. It is based on electrical stimulation from a pulse generate by a small device implanted in the neck. It is in the context of implantable devices able to sense and even actuate that this thesis will focus, mainly in the sensing aspect.

Due to the nature of ENG signals of few μV special attention must be taken in regards of noise, mainly on what concerns thermal noise. Not only that, external interferences are also responsible for degrading the desired ENG signal, where the most proeminent ones are EMG (electromyogram) artefacts, which might range from few μV up to mV. With these restrictions in mind, researches made with cuff electrodes are one of the first steps to be able to collect and process data from nerves, which are very sensitive regions with signals of extremely low amplitudes. Besides, it is fundamental to have an amplifying chain ensuring that the quality of the signal is preserved and amplified for further analysis.

The main goal of this thesis is to from an available instrumentation amplifier (IA) for ECG signals (designed by UCLouvain in 65 nm CMOS technology) build an adaptive tripolar configuration, with digitally-assisted gain tunability and low-power consumption for VENG (vagus-nerve ENG) signals.

The first contribution of this work was to modify the gain from the IA such that it could be digitally-tuned. This is essential for handling non-idealities present while using cuff-electrodes, where the growth of nerve, i.e, its adaptation to the cuff, generates imbalances in the way the signals are sensed, which can be corrected by modifying the gain accordingly. The methodology used to determine the number

of bits needed for the digital control comes from the specifications where the signal-to-interference ratio (ENG and EMG signals in this case) should be greater than 6 dB, for a range of impedance imbalance of ±40%, following [7].

The second was adapting the available IA to the ENG context, where the bandwidth of interest is no longer up to 250 Hz, but from 500 Hz to 10 KHz [30]. The last contribution was to implement the tripolar amplifier configuration for cuff electrodes by using the IA with gain tunability. Some of the results for the adaptive tripole were:

- Power = 13.5 μV
- SIR > 10 dB
- Range of imbalance correction: -40% to +40%
- Gain range: 36 dB to 44 dB (30 to 80 V/V)
- Gain resolution = 0.18 [V/V]

The simulations were performed in ELDO (SPICE environment) with the support of MatLab for analysis, calculations and graphs.

This thesis is organized as follows:

- Chapter 1 gives a description about what is epilepsy, main causes, symptoms and available treatments. It also highlights how seizure sensing is made and what are the relevant signals for this purpose.
- Chapter 2 explains about vagus nerve recording, since the source of the signals (how they are produced) up to its sensing, emphasizing the types of electrodes for ENG signals, what are the amplifier configurations with their advantages and drawbacks and a discussion about instrumentation amplifiers.
- Chapter 3 deals with the implementation with some metrics and how to deploy gain tunability for the IA from the specifications.
- Chapter 4 discusses the simulation results and the techniques implemented for dealing with non-monotonicity in the digital control when using binary code for the gain tunability from the IA, and, finally, comparisons between what was done in this work and the state-of-the-art.

Chapter 1

Epilepsy

It is a neurological disorder that affects around 50 million people worldwide [10] in which brain activities become abnormal, causing reactions more commonly seen as recurrent seizures, atypical behaviours and sensations and loss of awareness. Seizures can vary from short and almost undetectable periods to long ones of vigorous shaking and it might involve parts of the body (partial) or its entirety (generalized), as a consequence, can result in physical injuries, occasionally broken bones after loss of control during seizures.[19]

Despite of having seizures as the most noticeable feature for epileptic patients, seizure by itself does not mean epilepsy (around 10% of people worldwide have one crisis during their lifetime). In order to be recognized as epilepsy, a person must present two or more unprovoked seizures.

To better understand the effects from this condition and to identify what are the potential actions for it, in this chapter it will be highlighted its causes, symptoms, available treatments and the seizure sensing.

1.1 Causes

Many underlying disease effects can lead to epilepsy, however its cause is still unknown in about half of the registered cases. It is not contagious, but deserves special care. The causes are divided in categories: structural, genetic, infectious, metabolic, immune and unknown. Examples of known cases: brain damage from prenatal or perinatal causes (complications during birth), congenital abnormalities/genetic conditions with associated brain malformations, severe head injuries, strokes restricting amount of oxygen to the brain, brain tumors [19], and so on.

1.2 Symptoms

The main characteristic is the presence of seizures and depends on which region of the brain the disturbance starts and how it propagates. Temporary symptoms such loss of awareness, disturbances of movement, sensation, mood, or other cognitive functions are also present in these cases. People with epilepsy are more prone to physical (fractures and bruising related to crisis) and psychological conditions (e.g depression and anxiety), also they present higher risks of premature death (up to three times higher that average population). It is worth it to mention that a great proportion of deaths are preventable [19].

1.3 Treatments

Up to now there is no cure for epilepsy, however there are options for treatments. In this section, it will be given special attention to the most commonly used nowadays.

Medicine treatment (AED) Patients under this treatment use anti-epileptic drugs (AEDs), and it is the most common method for epilepsy, helping to control seizures in about 70% of people. They work by changing the chemical levels in the brain and despite of reducing the numbers of seizures, it does not cure epilepsy. There are different types of AED and they are chosen according to the person profile with epilepsy (type of seizures, age and interest of having a baby are some of them). AEDs are usually administered in tablets, capsules, liquids or syrups with daily use and, as all medicines, they might present side effects [18].

Brain surgery This method may be considered if AEDs are not enough for controlling the seizures and if they happen due to a problem in a small part of the brain that its removal would not cause serious effects. It is made by performing a small cut in the scalp and creating an opening in the skull allowing to remove the affected part of the brain. The recovery might take months to years still with the use of AEDs. This kind of surgery is always associated with risks, such as problems with memory, mood or vision and they might improve over time or be permanent.

Ketogenic diet It is a treatment for children (usually) or adults whose seizures are not controlled with AEDs. The diet may help to reduce amount and severity of seizures having other possible positive effects, it is very specialized needing proper supervision and guidance from medical advisors. The diet consists of high fat, low carbohydrate and controlled protein. The body normally uses glucose from carbohydrates for energy source. Chemicals called as ketones are generated when the body uses fat as source of energy (process known as ketosis). With ketogenic

diet, then, the body uses in most part ketones instead of glucose as energy source and some researches show that there are acids presented in this diet that contributes to control seizures. One drawback is constipation due to the lack of fibre, but with advices from nutritionist and other medical suggestions can be easily overcome [31].

Deep Brain Stimulation (DBS) DBS therapy is a surgical treatment used for reducing seizures not controlled with medication neither with surgery of part of the brain. It is made by implanting electrodes into specific areas of the brain and stimulating these regions with small regular electrical impulses. It is still a treatment under research. As can be seen in Figure 1.1a, it works by using a device called a neurostimulator that send electrical impulses to the brain. The electrodes are placed in the anterior nucleus of the thalamus, a part of the brain that is involved with the spread of seizures. For some people they have a warning or aura few moments before the seizure happens. When this happens, they can activate the DBS therapy immediately to try to stop a seizure event. To implement the whole system, it is also required surgery, leading to risks [31].

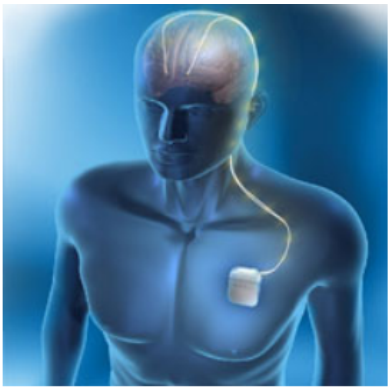

(a) Deep brain stimulation [2]

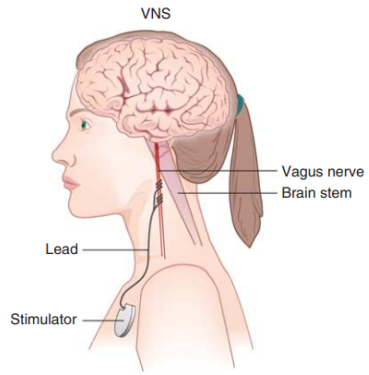

(b) Vagus nerve stimulation [23]

Figure 1.1: DBS and VNS treatments

Vagus Nerve Stimulation (VNS) VNS therapy is a treatment involving a stimulator (pulse generator) which is connected internally in the neck to the left vagus nerve. This generator produces regular electrical stimulations through this nerve helping to control irregular brain activities that lead to seizures. This therapy aims to reduce amount, period and severity of seizures, and it is a way for treating people whose seizures were not controlled with medication.

The vagus nerves are a pair nerves starting in the brain and going through the body, its location and distribution over the body are some of the reasons why it is an interesting part to apply stimulus.

For implementing, the stimulator is placed under the skin in the upper chest during a small operation and, then, a lead connects the stimulator to the vagus nerve in the left side of the neck, as shown in Figure 1.1b. The amount of stimulation varies from person to person, but it is common procedure to start at low levels and increase progressively up to a suitable level for the patient. Usually it is set at 30 seconds of stimulation every five minutes through day and night.

1.4 Seizure sensing

In order to visualize and collect relevant data regarding seizures, in this section it will be highlighted EEG (electroencephalogram), ENG (electroneurogram) and other signals.

1.4.1 EEG signals

With EEG, by positioning electrodes around the scalp of a patient, it is possible to observe the electrical signals produced for each region. In Figure 1.2 it is shown the behaviour of the recordings from a normal situation and then while a seizure. From that, features such duration and region of the brain under abnormal activity can be fetched. EEG signals are usually seen in the bandwidth between 0.5 Hz and 100 Hz, with amplitudes from dozens to hundreds of mV if measured from the scalp [16]. Depending on the predominant frequency seen, they might be classified as alpha, beta, gamma and delta waves useful for identifying abnormalities, for example.

Figure 1.2: (A) Normal EEG compared to (B) EEG including a seizure: epileptic seizure visible as rhythmic activity starting on electrodes P8 and T8 (from [11])

1.4.2 ENG signals

They can be used for detecting epileptic seizures, because some nerves (such as the vagus nerve) receive some indications about the seizure onset, since they induce visible physiological symptoms. Because of that, the vagus nerve is a key element for the traffic of information from the brain to other organs [28]. ENG signals present amplitudes is in the order of few μV [30] and have their bandwidth distributed over 500 Hz and 10 KHz, with peaks around 1 KHz and 3 KHz. A signal extracted from a rat can be seen in Figure 1.3.

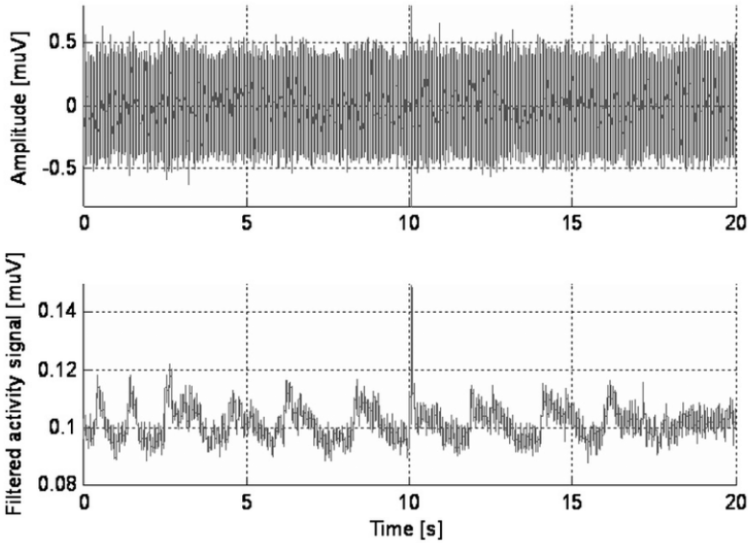

Figure 1.3: ENG signal of the rat sciatic nerve after mechanical stimulation of the paw: the raw and filtered signals. (from [14])

1.4.3 Other signals

Between other signals that affect the overall sensing there is, for example, the EMG (electromyogram) which amplitudes can reach mV order and the bandwidth is spread over 1 Hz and 3 KHz [30] usually more often concentrated at KHz range. Following similar nature, there is the ECG (electrocardiogram) signal also in the mV range and distributed over 1 Hz to 250 Hz. To summarize what was discussed in this section, see Figure 1.4.

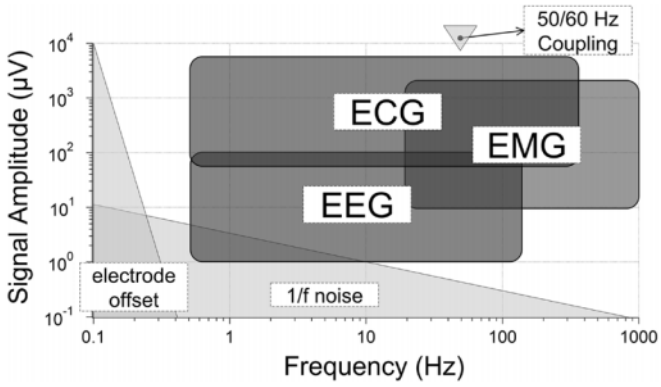

Figure 1.4: Frequency and amplitude characteristics of EEG, ECG, and EMG, and contaminating signals of the biopotential signals (not to scale) (from [34])

Chapter 2

Vagus nerve recording

In this chapter it will be presented how nerve signals are generated in the body along with how it is recorded nowadays, with special focus on vagus nerve because of its importance reflecting signals from the brain to other organs [28]. For nomenclature reasons, when the ENG signal is collected from the vagus nerve, it is called VENG (vagus nerve electroneurogram).

2.1 Electrical impulse & nerve recording

Electrical impulse One important event related to the electrical signals produced by the body is the action potential. Closely looking at the neuron, there is a voltage difference between its inside and the extracellular fluid, called resting potential (around -70mV). This voltage is caused by the sodium-potassium pump established by a chemical and electrical gradients.

For a recap, neurons are composed by dendrites, cell body and axons. The key to impulse conduction is the movements of ions inside and outside the membrane. If the summation of the signals from the dendrites of a neuron is sufficiently large, it can be observed an action potential, a pulse is produced and the membrane potential reaches the firing threshold (around -60 mV).

In the resting state, there are more relatively Na+ ions in the extracellular medium of the cell than the intracellular whereas the opposite happens with K+ ions. It is worth it to mention that this separation of ions creates a chemical gradient, while the presence of more positive particles outside the cell compared to the inside creates a electrical gradient. The membrane potential at rest is around -70mV, indicating that the inside of the cell is less positive than the outside. The axon, then, can be seen as having net positive charges in the outside and net negative charges in the inside at resting state.

Thus, with an action potential, there is a movement of ions allowed by ion

channel gates: rapid inflow of Na+ ions followed by an outflow of K+, rebalancing the membrane potential. This inflow of sodium ions depolarises that region of the membrane, causing it to keep following the same procedure and, as a consequence, the action potential propagates as a wave along the axon (when not myelinated), as can be seen in Figure 2.1, leading to impulse conduction. If myelinated, the impulse observes a "saltatory" conduction around the myelinated sheets, moving from node to node.

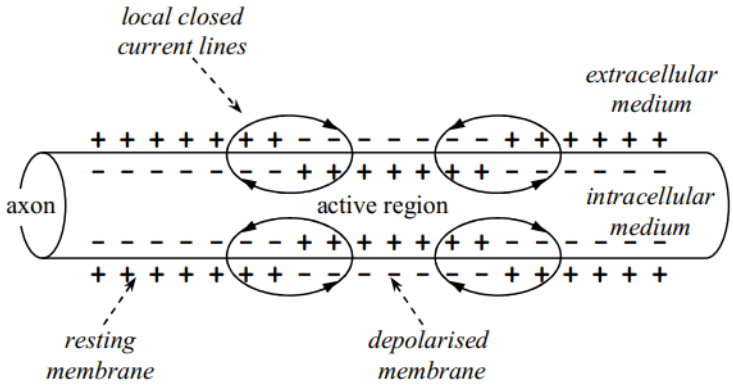

Figure 2.1: Neuron conduction when not myelinated (from [30])

The main goal is to be able to collect not a single action potential, but multiple ones, the field action potential usually from a nerve trunk (bundle), and for doing so, some different electrodes might be considered.

Requirements for nerve recording For biomedical applications, special attention should be given to the electrodes. They must fulfill certain requirements mainly when the interest is recording signals from a nerve. It should be able, for example, to perform properly for a long time span and offer minimal physiological or histological damage due to movements from the surroundings. There is one type called intrafascicular electrodes (needle electrodes penetrating the nerve, see Figure 2.2a): they provide relatively high ENG output signals, however, both are not widely spread for being invasive and potentially causing damages to the nerve in the long term.

For these reasons, the cuff electrode (Figure 2.2b) surrounding a nerve is more often used for not causing substantial internal harm to the nerve, despite of being less invasive [26] than intrafascicular electrodes. This thesis will focus on the cuff electrodes, being the main topic for discussion in the next sections.

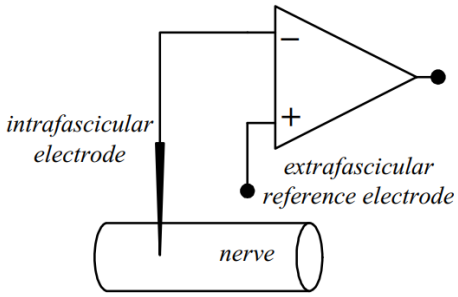

(a) Intrafascicular electrode compared to reference one in the nerve

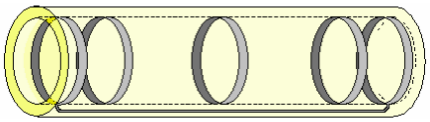

(b) Cuff electrodes

Figure 2.2: Types of electrodes (from [30])

Summarizing what was seen about electrodes, see Table 2.1. The terms invasive concerns if enters or not the body through a medical procedure. Intrusion is about the positioning: if inside the nerve then it is intrusive. Outside, non-intrusive.

Table 2.1: Comparison between intrafascicular and cuff electrodes

Electrode type	Invasive	Intrusive	Considerable damage in long-term	Output ENG signal
Intrafascicular	Yes	Yes	Yes	High
Cuff	Yes	No	No	Sufficiently high

2.2 Cuff electrodes

This type of electrode allows the implementation in patients for a reasonable amount of time, suitable for long-term applications. Available cuffs consist of insulating tubes made of biocompatible flexible insulating materials, as highlighted in [22], and the ring electrodes made of platinum-iridium or stainless steel attached to the interior wall of the cuff, covering almost the whole circumference (it has a gap for longitudinal opening in order to allow the nerve to be inserted in the cuff). A simplified scheme can be seen in Figure 2.3.

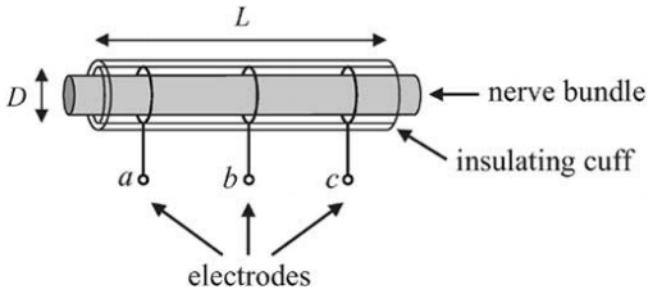

Figure 2.3: Cuff electrode surrounding the nerve trunk (from [21])

After the cuff is implanted, it is observed some changes in the nerve: sometimes growth tissue happens and due to local rearranging because of the cuff, the tissue may even cover the cuff, as can be seen in Figure 2.4 implanted in the nerve of a rat.

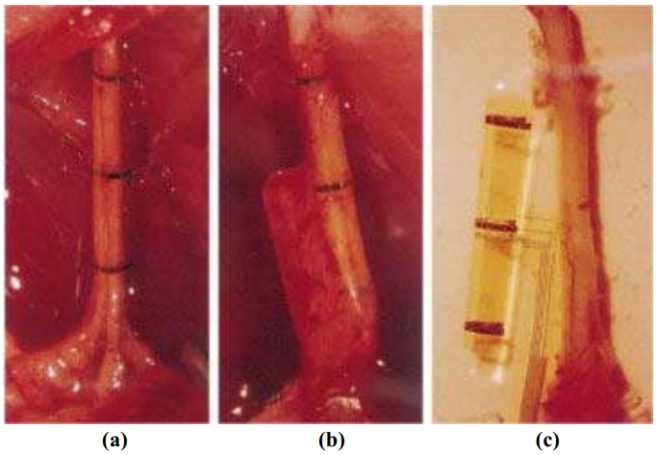

Figure 2.4: Cuff implemented in a rat (a), its progression with tissue adaptation (b), after removal of the cuff (c) (from [30])

2.2.1 Action potential inside the cuff

The neural signal obtained using cuff electrodes depends of some parameters, for example the slit closure, number of electrodes and presence of interference. Since the cuff surrounding a nerve bundle collects the activity from a group of axons, the recorded signal is the summation of the active potentials (field or compound active potential). In the literature, however, the studies with cuff electrodes were described in terms of single-fibre active potential, in order to be able to generalize to cover all types of nerve fibres.

As seen from [27] and [4], by modelling the Ranvier nodes as point current sources, the cuff observed signal is the sum of the contributions of all nodes inside it. These current sources are activated in sequence, since the action potential propagates along the fibre and its maximum amplitude reaches each node, producing i_{AC}. As a consequence, the same signal is observed in the cuff at different times multiplied by a scaling factor (weights), as can be seen in the Figure 2.5.

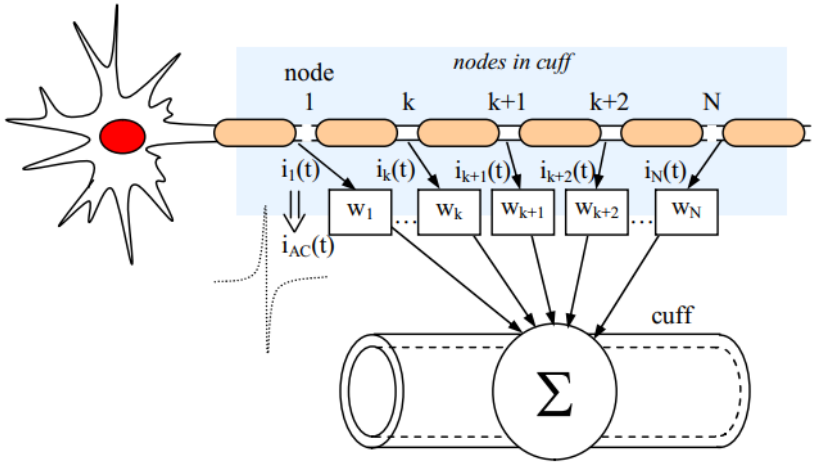

Figure 2.5: Schematic showing the contribution from the current sources at each Ranvier node (from [30])

As a result, the single-fibre action potential (SFAP) is given by:

$$SFAP(t) = \sum_{n=1}^{N} i_{AC}(x_n - ut) * w(x_n) \tag{2.1}$$

The weight function expressed in Ohms, is the voltage caused by the node n in position x_n in the cuff (measured by an electrode in the cuff), divided by the current of the node reaching the electrode. The weight profile in the cuff is shown in Figure 2.6, obtained experimentally from [3], where the maximum is observed in the middle of the cuff and, as result, the signal will follow the same shape, with the maximum amplitude in the middle of the cuff length.

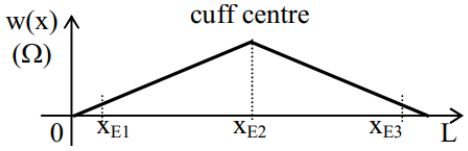

Figure 2.6: Cuff weighing function over the cuff (from [30])

2.2.2 Interferences & Cuff properties

The main source affecting the recorded ENG signals is the EMG interference. Due to the location of the nerves, these signals become very vulnerable to muscular contamination during recording where its amplitude can be up to three orders of magnitude larger. A common metric used for comparing both signals is the **SIR** (signal-to-interference ratio):

$$SIR = \frac{V_{ENG}}{V_{INT}} \tag{2.2}$$

Some of the most important advantages of using cuff electrodes are that the medium inside the cuff is only resistive (observing no significant phase differences to the interference potentials across the cuff electrodes) and the potential from external fields varies linearly with the distance inside the cuff (linearising property), as can be seen in the Figure 2.7. The last property will be broadly exploited in the interference reduction for the amplification chain aiming to record ENG signals.

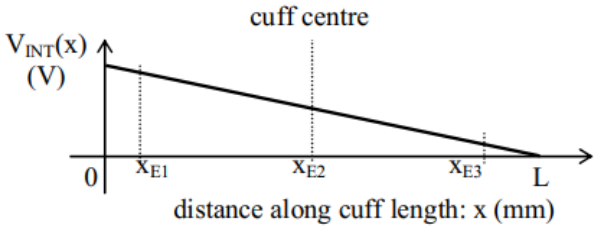

Figure 2.7: EMG external interference linearized inside the cuff (from [30], [25])

Assuming that the linear variation from external interference potentials $V_{INT}(x)$ are independent from the location of the external field, then, from Figure 2.7:

$$V_{INT}(x) = \alpha x + V_{INT}(0) \tag{2.3}$$

Here, the gradient α can be easily determined by using the potential at the end of the cuff:

$$\alpha = \frac{V_{INT}(L) - V_{INT}(0)}{L} \tag{2.4}$$

2.2.3 Cuff electrode configurations

In monopolar cuffs, the recording is done between a ring electrode inside the cuff and a reference one outside. The internal ring must be positioned as close as possible to the middle of the cuff to maximize the amplitude from the ENG signal.

In bipolar cuffs, the measurement is taken differentially between the two electrodes, with the signal level proportional to the separation between them. Finally, in tripolar cuffs, measurements are taken between the middle and the two other electrodes. These last ones positioned close to each end of the cuff to maximize the ENG signal. All these configurations can be seen in Figure 2.8.

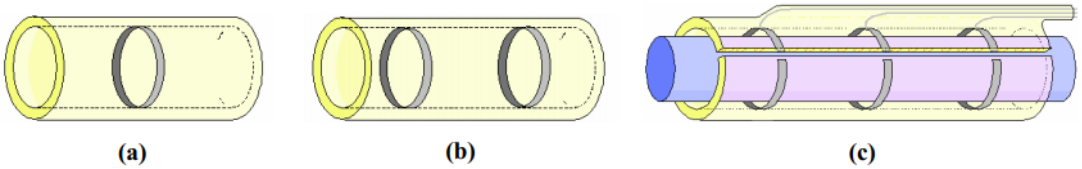

Figure 2.8: (a) Monopolar cuff, (b) Bipolar cuff and (c) Tripolar cuff electrodes from ([30])

In the study made in [24] it was shown that tripolar cuff electrodes provide better signal-to-interference ratio (SIR) and could be used in amplifying chains achieving greater interference reduction, as will be shown in further sections.

2.2.4 Ideal tripolar cuff model

Using the simplified model as shown in Figure 2.9, it is possible to analyze the impact of the EMG and ENG signals in terms of voltage and current. The description of each element in the model can be seen in the Table 2.2.

Points A, B and C are the output from the electrodes that will be used according to the amplifier configuration discussed in the next section and V_{ENG} is the desired signal. In the scheme, it is also shown not only the linearisation effect from external fields in the cuff, seen as the interference potential gradient, but also the ENG potential through the cuff as described in previous sections.

It is important to highlight that Z_{t_1} and Z_{t_2} correspond to the tissue impedance between the middle electrode and the other ones which will be relevant in the discussion of non-idealities, such as imbalance. In this ideal case, they have same values $Z_{t_1} = Z_{t_2} = 1.25k\Omega$. Also for the electrodes, they are assumed to have the same resistances.

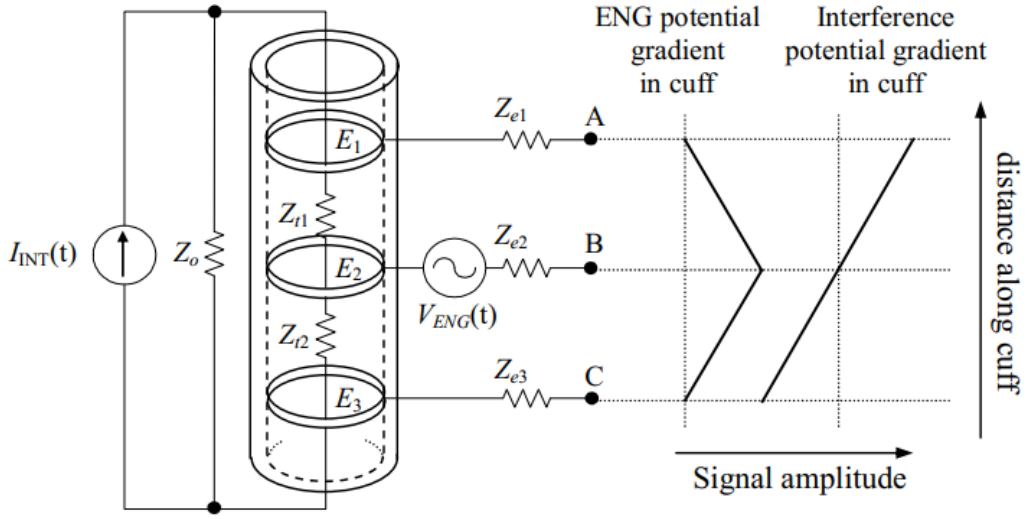

Figure 2.9: Ideal tripolar cuff model (from [7])

Element	Description	Value
Z_0	Tissue impedance outside the cuff	200Ω
$Z_t = Z_{t_1} + Z_{t_2}$	Tissue impedance inside the cuff	$2.5k\Omega$
$Z_{e_{1,2,3}}$	Electrode impedances	$1.0k\Omega$
I_{INT}	EMG interference signal	$1\mu A$

Table 2.2: Model elements description and nominal values (from [7], [30])

In this model, the current source I_{INT} will give rise to the interference voltages at V_{AB} and V_{BC} which are in anti-phase, while the ENG signal is in-phase, fact that will be explored in the amplifier configurations for obtaining great interference reduction.

2.2.5 Non-ideality: Impedance Imbalance

Among the non-idealities present in tripolar cuff, the impedance imbalance is one of the most important features that need to be taken care for recording ENG signal properly. It is the case when $Z_{t_1} \neq Z_{t_2}$ and it is usually computed in percentage as:

$$X_{imb} = \left(\frac{Z_{t_1} - Z_{t_2}}{Z_t}\right) * 100\% \tag{2.5}$$

This also allows the computation of $Z_{t_{1,2}}$ in terms of X_{imb}:

$$Z_{t_1} = \frac{Z_t(1 + X_{imb})}{2} \tag{2.6}$$

$$Z_{t_2} = \frac{Z_t(1 - X_{imb})}{2} \tag{2.7}$$

Causes Two known causes of imbalance are cuff asymmetry, when the electrode placement is imperfect usually from manufacturing deviations, and the inhomogeneous tissue growth after implantation of the cuff, as shown in Figure 2.4 (b). In the ideal model, the assumption $Z_{t_1} = Z_{t_2}$ means that the cuff is totally symmetrical and with tissue uniformly distributed inside the cuff, however, these behaviours are not achieved in real implanted cuffs. The imbalance issue can be addressed by some specific amplifier configurations and will be studied in the next section.

2.3 Tripolar amplifier configurations

The amplifier configurations used along with tripolar cuff electrodes are the quasi-tripole (QT) and the true-tripole (TT), as shown in Figure 2.10. In both cases it is exploited the ability to cancel the EMG interference by using the linearising property from external fields inside the cuff. Assuming the cuff is symmetrical, the EMG signal is expected to be cancelled and only the ENG signal is observed at the output from these architectures.

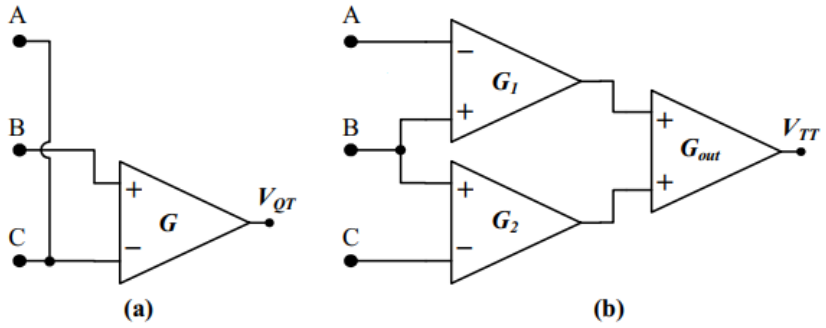

Figure 2.10: Quasi-tripole (a) and True-tripole configurations (b) (from [29])

By using these configurations along with the cuff model previously seen in Figure 2.9, it is possible to determine the impact of the interfering EMG signal at the output.

2.3.1 Quasi-Tripole

By grouping the cuff model along with the amplifying configuration (see in Figure 2.10 (a), following the nomenclature in Figure 2.10 and ignoring the ENG contribution, it is obtained: (V_X is the node between Z_0 and Z_{t_1}, moreover: $Z_{e_1} = Z_{e_3} = Z_a$)

$$V_{QT} = G(V_B - V_C) \tag{2.8}$$

$$V_A = V_C = \frac{V_X}{2} \tag{2.9}$$

$$V_B = V_X \frac{Z_{t_2}}{Z_t} \tag{2.10}$$

$$V_X = I_{INT} Z_0 \frac{Z_t // 2Z_a}{Z_t // 2Z_a + Z_0} = I_{INT} \frac{2Z_0 Z_t Z_a}{2Z_t Z_a + Z_0 Z_t + 2Z_0 Z_a} \tag{2.11}$$

From (2.11) into (2.9) and (2.10) and replacing in (2.8):

$$V_{QT} = G \frac{I_{INT} Z_0 (Z_{t_2} - Z_{t_1})}{2Z_t + 2Z_0 + \frac{Z_0 Z_t}{Z_a}} \tag{2.12}$$

2.3.2 True-Tripole

In this case it will be used the configuration in Figure 2.10 (b) and, by using a similar approach as the Quasi-Tripole and considering V_C as the reference node, it yields:

$$V_{TT} = G_{out}[G_1(V_B - V_A) + G_2(V_B - V_C)] \tag{2.13}$$

$$V_A = Z_0 I_{INT} \frac{Z_t}{Z_0 + Z_t} \tag{2.14}$$

$$V_B = V_A \frac{Z_{t_2}}{Z_t} \tag{2.15}$$

$$V_C = 0 \tag{2.16}$$

From (2.14), (2.15) and (2.16) into (2.13):

$$V_{TT} = G_{out} \frac{Z_0 I_{INT} (G_2 Z_{t_2} - G_1 Z_{t_1})}{Z_0 + Z_t} \tag{2.17}$$

One important point to mention is that the ENG signal will pass through each amplifier and then will be summed up. As a result, the ENG signal at the output in the TT configuration is given by:

$$V_{ENG_{TT}} = G_{out}(G_1 + G_2) V_{ENG}^{in} \tag{2.18}$$

2.3.3 Comparison

Comparing equations (2.12) and (2.17), the residual output interferences due to the EMG signal are dependent on $(Z_{t_2} - Z_{t_1})$ in the QT configuration and on $(G_2 Z_{t_2} - G_1 Z_{t_1})$ in the TT, showing that in the first the condition for no-interference would be $Z_{t_2} = Z_{t_2}$, achieved only in the ideal cuff case, limiting its use when non-idealities such impedance imbalance are presented. In contrast, the TT has the possibility of adjusting the gains G_1 and G_2 so that even if $Z_{t_1} \neq Z_{t_2}$ there is a combination G_1, G_2 such that $V_{TT} = 0$. By rewriting the equations (2.12) and (2.17) in terms of X_{imb}, it yields:

$$V_{QT} = \left(-G \frac{I_{INT} Z_0 Z_t}{2Z_t + 2Z_0 + \frac{Z_0 Z_t}{Z_a}} \right) X_{imb} \tag{2.19}$$

$$V_{TT} = \left(-G_{out} G \frac{I_{INT} Z_0 Z_t}{Z_0 + Z_t} \right) X_{imb} \tag{2.20}$$

In equation (2.20), it was considered that $G_1 = G_2 = G$. Assuming $G_{out} = 1$, it can be seen that for no-imbalance, both results are zero. When there is imbalance, V_{TT} is larger than V_{QT}, in other words, the SIR of QT is better than in TT configuration for the same ENG level, however, the latter has the possibility to correct imbalances externally by adjusting the gains.

In terms of noise, in the paper [20], it was shown that true-tripolar configurations present higher SNR (ENG) compared to quasi-tripolar under the same conditions, see Figure 2.11, reinforcing some of the advantages of TT over the QT. In the same time, additional circuitry is demanded potentially occupying larger area and consuming more power when designed on chip.

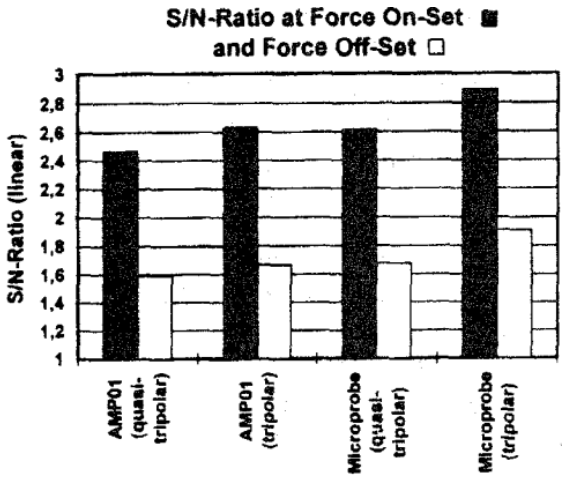

Figure 2.11: Comparing QT and TT configurations for 2 types of amplifiers (AMP01 and MicroProbe) (from [20])

2.3.4 Adaptive-Tripole

With the concepts of QT and TT in mind, the adaptive-tripole (AT) is an evolution from the TT where the possibility of removing imbalance is finally implemented and with tunable gain for dealing with such non-ideality, increasing the SIR and the ENG signal quality. In [7], it was shown one way to compensate the imbalance by using a fully-analog architecture as shown in Figure 2.12. It uses 1) low-noise preamplifiers, 2) gain-adjustable OTAs, 3) rectifiers, 4) comparator and an 5) integrator. For the adjustable-gain OTA, the current after the integrator is fed back to the OTA, changing the tail-current and, as such, modifying the gain according to the imbalance seen.

In [7] they were able to achieve $SIR_{out} > 6dB$ for an imbalance correction range of more than 40% and input-referred noise of 290 nV_{rms} for a bandwidth from 1 Hz to 15 KHz at the expense of 7.2 mW. In this paper, an AT will also be designed but with digitally-controlled gain as will be seen in a specific section.

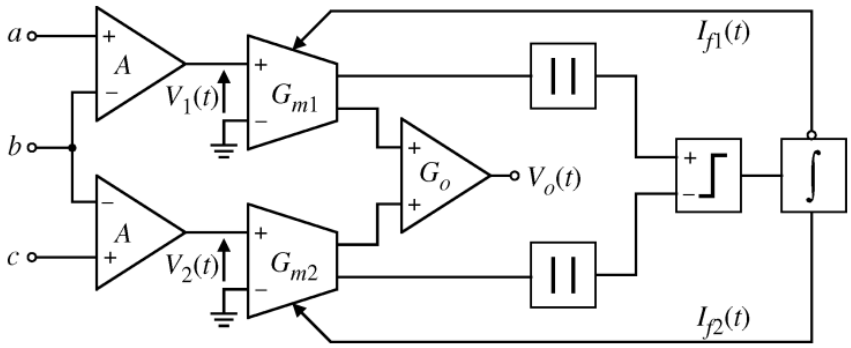

Figure 2.12: Adaptive-tripole architecture (from [7])

In order to implement the AT configuration, it is needed to have an instrumentation amplifier respecting certain prerequisites while acquiring biomedical signals. For that, a detailed analyze of it will be presented.

2.4 Classic Instrumentation Amplifier

For biomedical applications, the main design specifications for instrumentation amplifiers (IA) are high CMRR (rejecting mains interference), high input impedance (minimizing effect of electrode mismatches), low input-referred noise, low power consumption and potential to reject high levels of DC-electrode offset. In this thesis it will be exploited the Current-mode instrumentation amplifier (CMIA) by first showing its advantages over the classic IA (3-OpAmp IA) and then, how to assemble it into the desired architecture of true-tripole.

As seen in Figure 2.13, one of the main advantages from this configuration comes from the **high input impedance**, directly connected to the input of an opamp. In order to analyze its other features, the circuit will be splitted into 2 parts, as seen in Figure 2.14.

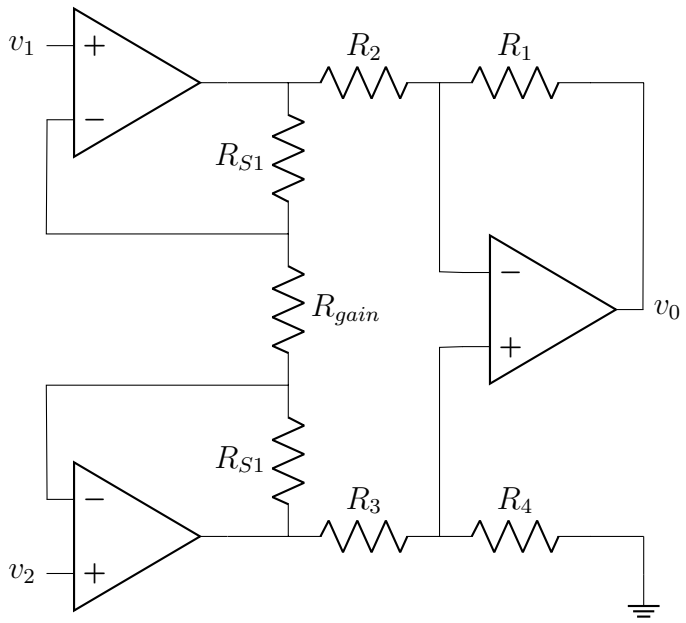

Figure 2.13: The classic 3 OpAmp IA

2.4.1 CMRR

In order to see what is the CMRR from the 3 OpAmp IA, this value will be calculated for part 1 and part 2.

Part 1 By applying V_{CM} at both inputs, assuming each opamp is ideal, the current across R_G is zero because both terminals follow the V_{CM}. As a consequence, $v_{01} = v_{02} = v_{cm}$ and it produces $A_{CM} = 1$. Now, by applying $\frac{+v_{diff}}{2}$ and $\frac{-v_{diff}}{2}$ to v_1 and v_2, respectively, it yields:

$$\begin{aligned} i &= \frac{v_{diff}}{R_{gain}} = \frac{v_{01} - v_{02}}{2R_{S1} + R_{gain}} \\ A_{d_1} &= \frac{v_{01} - v_{02}}{v_{diff}} = \frac{2R_{S1} + R_{gain}}{R_{gain}} \end{aligned} \tag{2.21}$$

As a consequence, for the first stage:

$$\begin{aligned} CMRR_1 &= \frac{A_{d_1}}{A_{CM_1}} \\ CMRR_1 &= \frac{2R_{S1} + R_{gain}}{R_{gain}} \end{aligned} \tag{2.22}$$

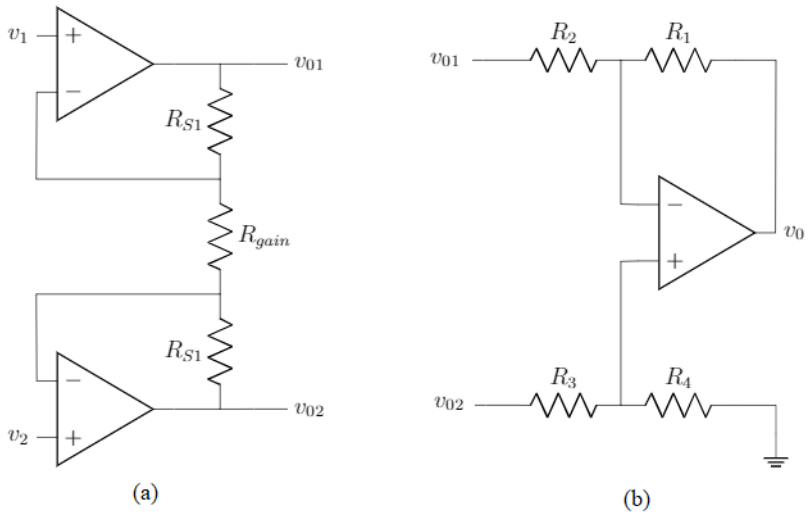

Figure 2.14: (a) Part 1 and (b) Part 2

Part 2 Using Figure 2.15 a), it is obtained, for the common-mode:

$$V_B = v_{CM}\left(\frac{R_1}{R_1+R_2}\right) + v_0\left(\frac{R_2}{R_1+R_2}\right) \tag{2.23}$$

$$V_A = v_{CM}\left(\frac{R_4}{R_3+R_4}\right) \tag{2.24}$$

$$V_A = V_B \tag{2.25}$$

From (2.24) and (2.23) to (2.25):

$$A_{CM_2} = \frac{v_0}{v_{CM}} = \frac{\left(\frac{R_4}{R_3+R_4} - \frac{R_1}{R_1+R_2}\right)}{\left(\frac{R_2}{R_1+R_2}\right)} \tag{2.26}$$

Now, for the differential gain:

$$V_A = \frac{v_{diff}}{2}\left(\frac{R_4}{R_3+R_4}\right) \tag{2.27}$$

$$V_B = -\frac{v_{diff}}{2}\left(\frac{R_1}{R_1+R_2}\right) + v_0\left(\frac{R_2}{R_1+R_2}\right) \tag{2.28}$$

From (2.27) and (2.28) to (2.25):

$$A_{d_2} = \frac{v_0}{v_{diff}} = \frac{\left(\frac{1}{2}\right)\left(\frac{R_1}{R_1+R_2} + \frac{R_4}{R_3+R_4}\right)}{\left(\frac{R_2}{R_1+R_2}\right)} \tag{2.29}$$

Finally, by using $CMRR_2 = \frac{A_{d_2}}{A_{CM_2}}$, with further simplifications:

$$CMRR_2 = \frac{\left(\frac{1}{2}\right)\left(\frac{R_1}{R_1+R_2} + \frac{R_4}{R_3+R_4}\right)}{\left(\frac{R_4}{R_3+R_4} - \frac{R_1}{R_1+R_2}\right)} \tag{2.30}$$

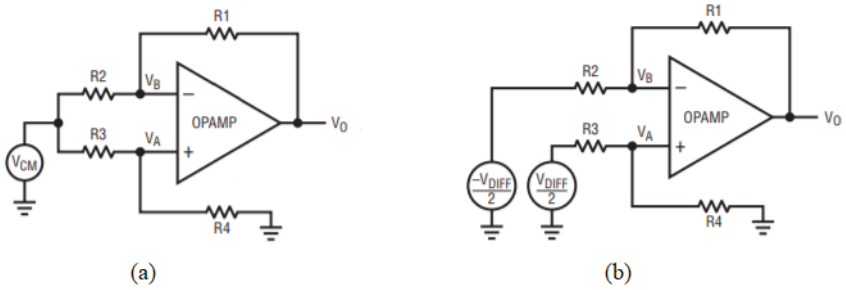

Figure 2.15: (a) Part 2 for common-mode gain and (b) Part 2 for differential gain

Despite of using the ideal opamp for this analysis, from equations (2.22) and (2.30), it can be seen that the CMRR relies on matching of resistors, with the second part as an example of that. Therefore, the global CMRR is dominated by the CMRR from the second stage, mainly in what concerns the ratio $\frac{R_3}{R_4}$ and $\frac{R_2}{R_1}$. The best case scenario is $\frac{R_3}{R_4} = \frac{R_2}{R_1}$, when the CMRR would be as high as possible.

2.4.2 Power vs noise

The opamp used in this configuration can be seen as a two-stage miller OTA, as shown in Figure 2.16a. Then, in order to calculate the impact from the noise, it is needed to observe the impact of each transistor at the output.

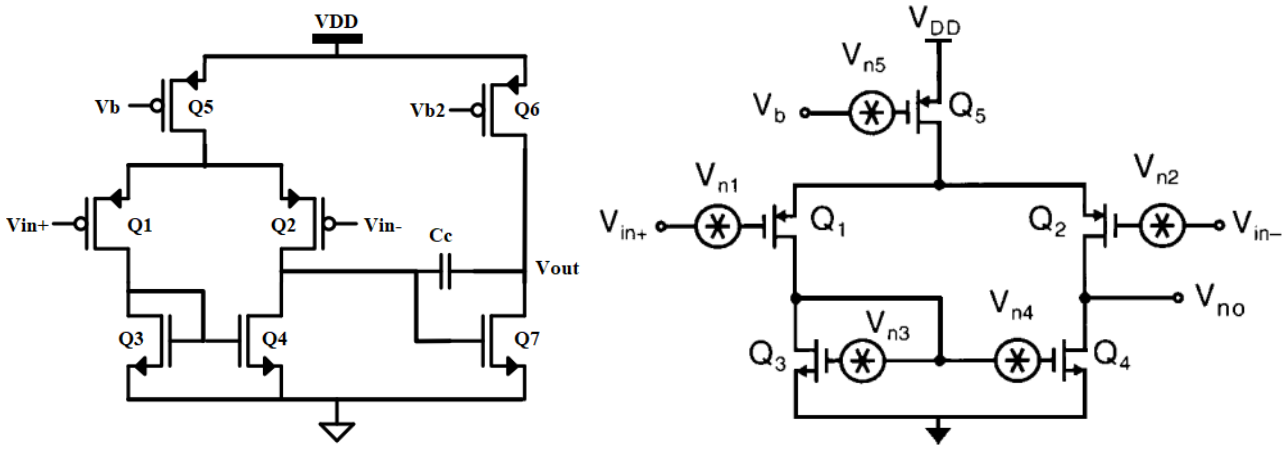

(a) 2-Stage Miller OTA **(b) Noise in input stage**

Figure 2.16: Miller OTA and its noise in input stage

Introducing R_0 as the output impedance at node V_{no} in Figure 2.16b, the gain of each transistor with respect to the output can be seen as:

$$\left|\frac{V_{no}}{V_{n1}}\right| = \left|\frac{V_{no}}{V_{n2}}\right| = g_{m1}R_0 \tag{2.31}$$

$$\left|\frac{V_{no}}{V_{n3}}\right| = \left|\frac{V_{no}}{V_{n4}}\right| = g_{m3}R_0 \tag{2.32}$$

$$\left|\frac{V_{no}}{V_{n5}}\right| = \frac{g_{m5}}{2g_{m2}} \tag{2.33}$$

Here it was assumed that the pairs (Q1,Q2) and (Q3,Q4) are matched. Then, it is possible to obtain the equivalent output noise voltage, and then, by dividing by the global gain $g_{m1}R_0$, the input-referred noise:

$$V_{no}^2(f) = 2(g_{m1}R_0)^2V_{n1}^2(f) + 2(g_{m3}R_0)^2V_{n3}^2(f) + \left(\frac{g_{m5}}{2g_{m2}}\right)^2 V_{n5}^2(f) \tag{2.34}$$

$$V_{irf}^2(f) = 2V_{n1}^2(f) + 2V_{n3}^2(f)\left(\frac{g_{m3}}{g_{m1}}\right)^2 \tag{2.35}$$

The noise contribution from Q5 can be neglected, since it is very smaller compared to the other terms, already simplified in equation (2.35). The noise from a MOS transistor can be seen as a contribution from the thermal noise and the flicker noise. The equivalent noise seen at the gate of a MOS transistor is shown

below, with the first term being the thermal and the second the flicker noise.

$$V_i^2(f) = 4KT\left(\frac{2}{3}\right)\left(\frac{1}{g_{mi}}\right) + \frac{K_i}{W_i L_i C_{ox} f} \tag{2.36}$$

$$g_{mi} = \sqrt{2\mu_i C_{ox}\left(\frac{W_i}{L_i}\right) I_{D_i}} \tag{2.37}$$

By replacing (2.36) into (2.35), the V_{irf} divided on its components already simplified can be seen as:

$$V_{irf}^2(f) = V_{th}^2 + V_f^2 \tag{2.38}$$

$$V_{th}^2 = \frac{16}{3}KT\left[\frac{1}{g_{m1}} + \left(\frac{g_{m3}}{g_{m1}}\right)^2 \frac{1}{g_{m3}}\right] \tag{2.39}$$

$$V_f^2 = \frac{2}{C_{ox}}\left[\frac{K_1}{W_1 L_1} + \left(\frac{\mu_n}{\mu_p}\right)\left(\frac{K_3 L_1}{W_1 L_3^2}\right)\right] \tag{2.40}$$

From (2.39), one way to reduce the thermal noise is to increase g_{m1}, by increasing I_{D_1} and, I_{D_5} that generates the biasing current from the circuit. From here it can be seen a trade-off between noise and power from the input stage $P = V_{DD} I_{D_5}$.

For the flicker noise, increasing L_3 would be a good solution to reduce its impact, but paying attention to the signal swing. Other alternative is the chopper modulation, that will also be discussed in further sections.

For the output stage, in Figure 2.13 it can be seen that the opamp must drive the resistor R_{gain} and, by knowing the noise in the resistor $\bar{V}_{R_n} = 4KTR_{gain}\Delta f$, it is needed to minimize R to minimize the noise, but from $V_R = RI_{D_6}$ it would be needed a large I_{D_6}, demanding a large power output stage. It is also important to mention that changing R_{gain} also impacts the global gain ($A = A_{d_1} A_{d_2}$), because A_{d_1} depends on R_{gain}.

As a summary, the 3 OpAmp for noise considerations must have large input power and large output power.

2.5 Current-Mode Instrumentation Amplifier

This configuration can be seen as 2 different stages: the first composed by two input op amps and a resistor R_1. The op amps are connected as unit gain buffers, with the input voltage across R_1. Like this, only differential current $i = \frac{v_1 - v_2}{R_1}$ flows over R_1. In the second stage, by using mirroring techniques, this current is collected and the output voltage observes the same i but over R_2, i.e, $v_{out} = (v_1 - v_2)\frac{R_2}{R_1}$. It also presents **high input impedance** since it is directly connected to an op amp.

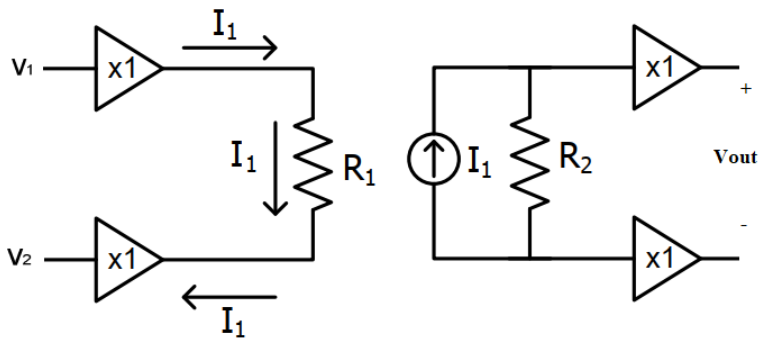

Figure 2.17: Current-Mode IA scheme: current copied into second stage ([13])

2.5.1 CMRR

Differently from the 3-Opamp configuration, here the CMRR relies on matching of the buffers used, as it was shown in [15], where, assuming the range of frequencies to be work on below the cut-off frequency:

$$\frac{1}{CMRR_{IA}} \approx \frac{1}{A_{d_2}} - \frac{1}{A_{d_1}} + \frac{1}{CMRR_1} - \frac{1}{CMRR_2} \tag{2.41}$$

Where A_{d_1} and A_{d_2} are the differential gains from the buffers followed by their CMRRs. From (2.41) it can be seen that the differential gains must be as high as possible, with well matched op amps in order to obtain high CMRR. This architecture explores another way to obtain high CMRR without relying on resistor network matching.

2.5.2 Power vs noise

By taking a look at Figure 2.17, the noise sources will be the buffer voltages and R_1 for the input stage and the voltage buffers and R_2 for the output stage. Then, in a simplified way, and knowing that the gain is $A = \frac{R_2}{R_1}$, the input-referred noise can be calculated as (with the $\bar{v}^2_{BUF}$ as the buffer noise contribution):

$$\bar{v}^2_{IRF}(f) = 2\bar{v}^2_{BUF}(f) + 4KTR_1\Delta f + \frac{4KTR_2\Delta f}{A^2} + \frac{2\bar{v}^2_{BUF}(f)}{A^2} \tag{2.42}$$

The noise is dominant in the first stage, since the contributions from the second are divided by the gain squared.

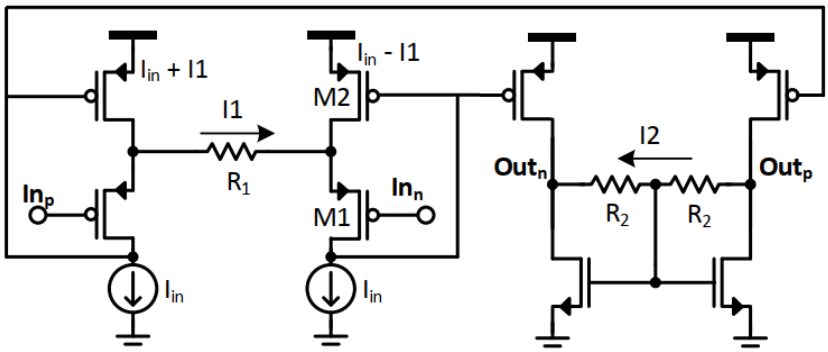

Figure 2.18: Current-Mode IA example [13]

From the Figure 2.18, it can be seen that R_1 is driven by the input stage, contrary to what happened to the 3-OpAmp configuration. The main advantage comes from the fact that this mode does not require high-power output stage to produce low noise, being the most suitable alternative when low-power is striven for. There are some methods used for reducing the noise, such as the chopper modulation as will be seen in the following section.

2.6 Chopper modulation technique

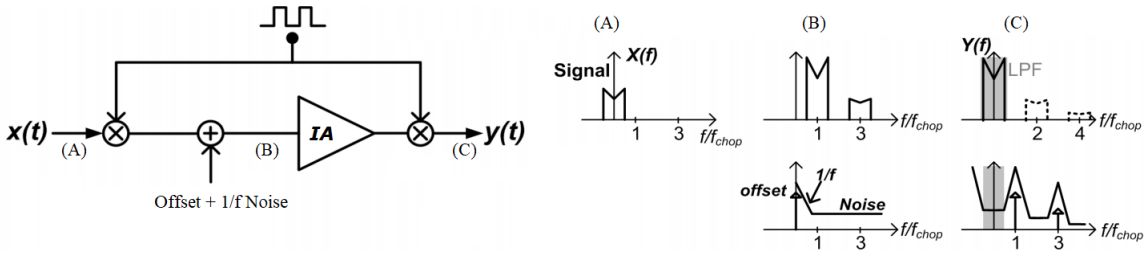

Figure 2.19: Chopper modulation [13]

Application It is a technique commonly used for removing DC offsets from amplifiers due to some mismatches and also as an approach to reduce the impact from flicker noise in signals working in the bandwidth where its influence is proeminent. In this case, for example, suitable for bio-applications where the signals are usually spread over lower frequencies.

Principle The idea behind is to play with modulation by a square wave of higher frequency compared to the signal, by separating the non-idealities band from the

signal. An illustration is shown in Figure 2.19, in which the bands are splitted and with a further use of a low-pass filter, these effects are reduced. The implementation can be made by using switches as can be seen in Figure 2.20.

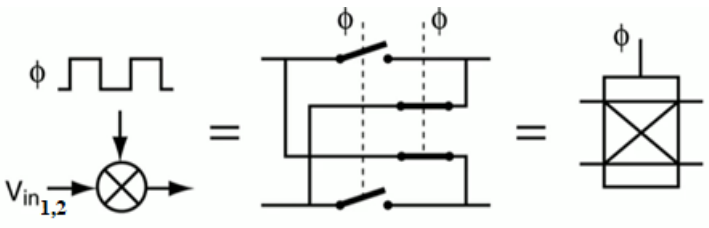

Figure 2.20: Chopper modulation done by switches

Drawbacks One of the problems concerns the bandwidth of the amplifier in use, that must be able to deal with the chopped signal, demanding high bandwidth amplifiers compared to the original signal. Another point is the clock feedthrough and charge injection leading to residual offsets due to the parasitic capacitances, important when the design uses switches, as shown in Figure 2.21. It is also important to mention that it reduces the input impedance, since the switches, connected to load capacitances, will work as switched-capacitors.

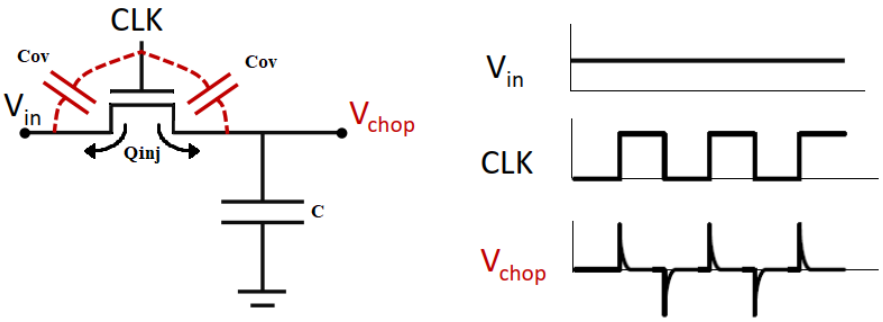

Figure 2.21: Clock feedthrough and charge injection due to parasitic capacitances

Chapter 3

Implementation

In this chapter it will be shown 1) the starting point from an available IA from UCLouvain and its figures of merit, then 2) the changes needed to be done in order to satisfy the requirements for ENG sensing followed by a brief description of how the circuit works and, finally, 3) how to make use of the circuit for an adaptive-tripole which main goal resides on dealing with impedance imbalances. The last 2 are the main contributions from this thesis.

3.1 Fully-differential current-mode instrumentation amplifier

The instrumentation amplifier in use was based on [33] and uses a fully-differential CMIA. It was an available IA previously designed by UCLouvain and because of that, it was the chosen IA to start working with. Since initially it was used for ECG applications, in order to achieve the requirements for ENG signals, some changes must be made.

Adaptation to ENG sensing This architecture aimed to collect ECG signals, which signals range from 1 Hz to 300 Hz. As such, the original bandwidth of the IA (around 300 Hz) suffered substantial influence of flicker noise. For the IA of this thesis, there were 3 main modifications: the first to modify the bandwidth for around 10 KHz, where the ENG signals are found. This was simply done by reducing the capacitance value responsible for the filtering. The second was removing the choppers, for some reasons: 1) the ENG signals are distributed from 500 Hz to 10 KHz and in order to modulate signals at a higher chopping frequency it would be needed an IA with a large bandwidth reducing the output capacitance, being affected when further stages are connected to it; 2) parasitic capacitances provoke charge injection that affect the output and the quality of the signals; 3)

the flicker noise dominates for lower frequencies and from the noise distribution it can be seen that the ENG bandwidth does not lie in those frequencies (see Figure 3.5). The third major change concerns the gain-tunability and a special session will be dedicated to discuss it. For the next calculations only the 2 first changes described here will be used.

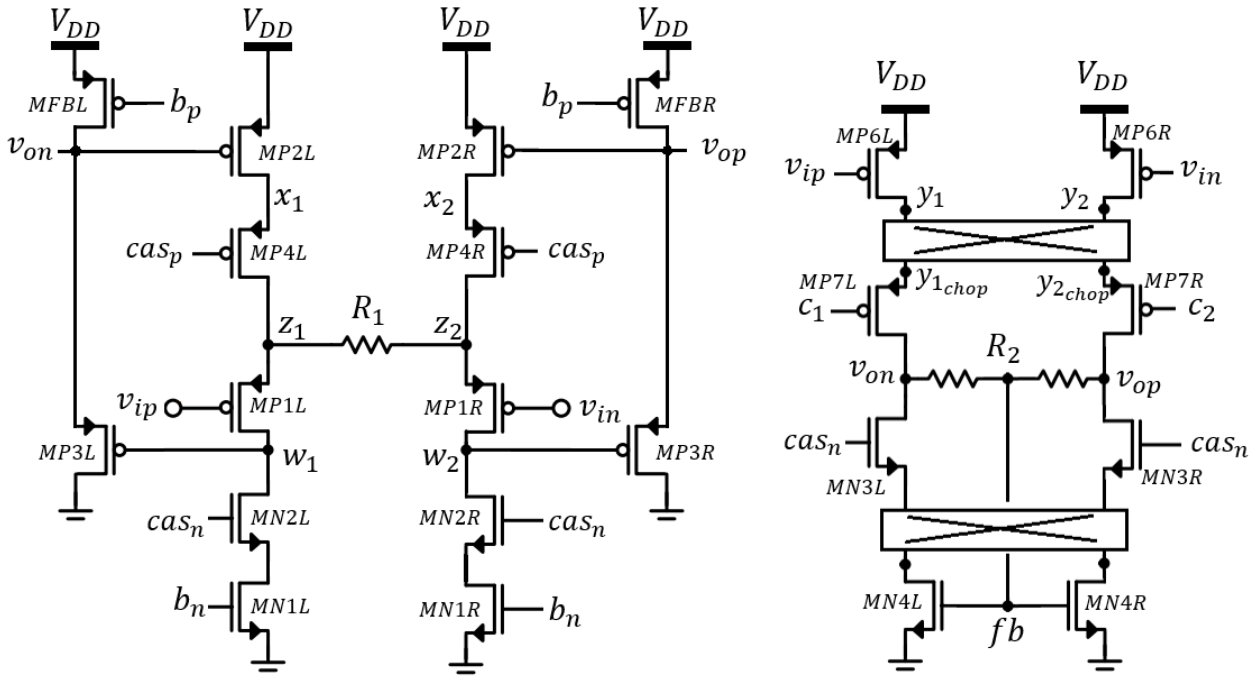

(a) Transconductance stage **(b) Transimpedance stage**

Figure 3.1: Input and output stages from the CMIA (from [33])

Circuit description The circuit is composed by 2 main stages: the Gm (transconductance input stage) and the TI (transimpedance output stage), as they can be seen in Figure 3.1a and Figure 3.1b, respectively. Here $v_{op,n}$ from Gm-stage are connected to $v_{ip,n}$ from TI-stage. It is important to mention that the inputs from Gm-stage considered passed through first a high-pass filter (HPF) with $f_c = 0.5Hz$ and then by a chopper block with $f_{chopper} = 4000Hz$. For this reason, in the original architecture, the input stage deals with a modulated signal.

The voltages $cas_{n,p}$ and $b_{n,p}$ are the ones used for cascoding and biasing. As described previously in the discussion of CMIA, the transistor MP1L is working as voltage follower from the input to z_1, analogously for the right-side. The current generated in each branch is then copied through the current mirror pair MP2L and MP6L, scaled by current mirror ratio. One possible problem could arise if the common-mode input voltages are large, consequently increasing the voltage at z_1

leading MP2L to triode region and, as such, the current from the current mirror (MP6L) would no longer be the copy from the Gm-stage, generating distortion and reducing the CMRR. As an alternative, 2 amplifiers are added collecting the voltages at nodes (x_1, y_2) and (x_2, y_1) and feeding the output after chopping to to MP7L and MP7R, regulating the current mirror.

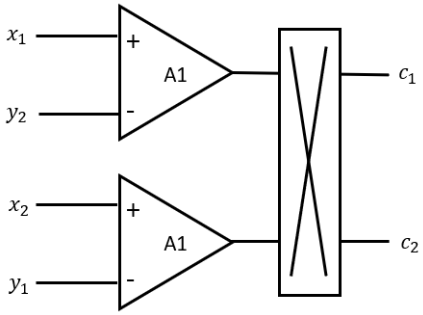

Figure 3.2: Amplifiers A1 added to regulate the current mirror [33]

From the paper [32], it was shown that the gain of this circuit can be approximated to:

$$A \approx a_{CM} \frac{R_2}{R_1} \tag{3.1}$$

$$a_{CM} = \frac{\left(\frac{W}{L}\right)_6}{\left(\frac{W}{L}\right)_2}$$

From this gain equation it is possible to obtain some insights of how to make the circuit with variable gain. Since R_2 and R_1 are usually the polysilicon resistances, the a_{CM} could be tuned to generate this variable gain behavior, as will be exploited later.

The sizes can be seen in Table 3.1, where the M values are the amount of transistors in parallel for increasing the overall W.

Table 3.1: Sizes from Gm and TI stages (L and R omitted)

Transistors	(W/L) $[\mu m/\mu m]$	M
MP2	2.25/10	6
MP4	1.5/5	6
MP1	80/5	10
MN2	37.8/10	6
MN1	12.6/20	6
MP3	0.12/20	1
MFB	0.9/10	1

Transistors	(W/L) $[\mu m/\mu m]$	M
MP6	1.9/10	3
MP7	0.75/5	3
MN3	18.9/10	3
MN4	6.3/20	3

3.1.1 Input impedance & CMRR

Since the input is connected to the gate of a transistor, the input impedance is mainly dependent on the capacitances in the region. From simulation, the obtained result was $Z_{in} = 177M\Omega$ at 50 Hz.

The CMRR was obtained by running MonteCarlo simulation in order to see the impact of mismatches in the gains. For comparing the common-mode and differential gains, the total number of runs (per type of gain) was 500 and the results can be seen in Figure 3.3 and Figure 3.4.

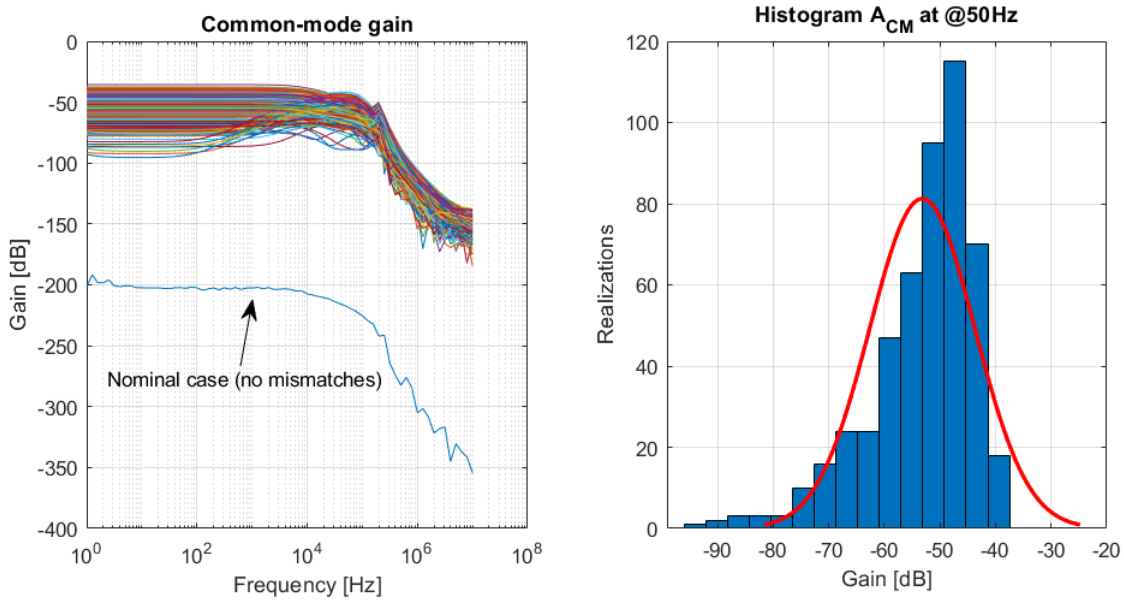

Figure 3.3: Common-mode gain and its histogram

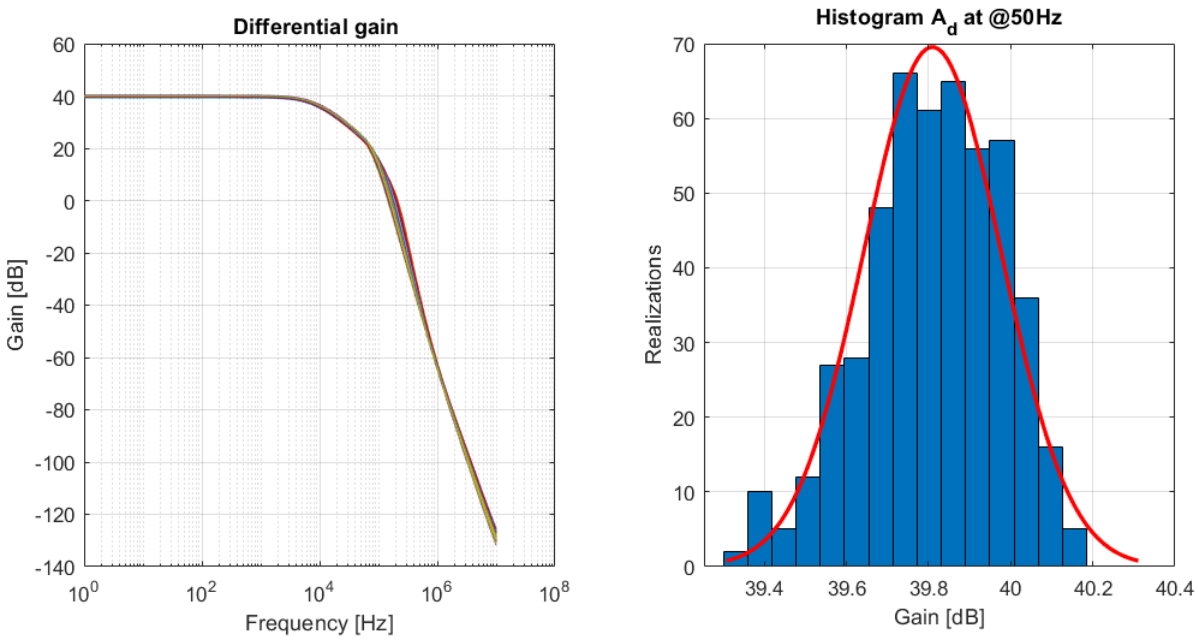

Figure 3.4: Differential gain and its histogram

Picking up the gains at $f = 50Hz$ from the mains, the worst case scenario is obtained for the lowest A_d and largest A_{cm}. From that:

$$\begin{aligned} CMRR_{dB_{50Hz}} &= A_{d_{dB}} - A_{cm_{dB}} \\ CMRR_{dB_{50Hz}} &= 39.3 - (-35.7) \\ CMRR_{dB_{50Hz}} &= 75dB \end{aligned}$$

Using the statistical mean (not the one from the histograms)

$$\begin{aligned} CMRR_{dB_{50Hz}} &= 39.8 - (-49.4) \\ CMRR_{dB_{50Hz}} &= 89.2dB \end{aligned}$$

It is safe to assume, then: $CMRR_{dB_{50Hz}} \geq 75dB$.

3.1.2 Power vs noise

For the noise, it was taken the input-referred noise and its spectral distribution, that allows the calculation of the $V_{n_{RMS}}$ from the graph. In can clearly be seen in the log-log plot the flicker noise contribution and the thermal noise level, as highlighted in Figure 3.5. The corner frequency found was $f_c = 147Hz$ and the thermal noise floor was $30\frac{nV}{\sqrt{Hz}}$.

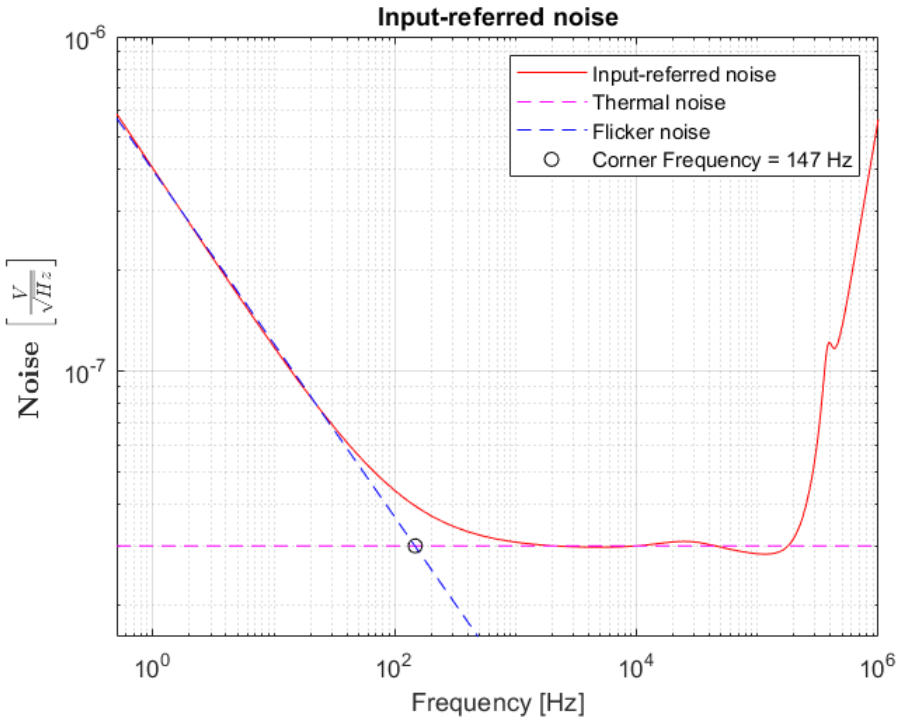

Figure 3.5: Input-referred noise spectral distribution

From Figure 3.5, it was calculated the $V_{n_{RMS}}$ using $f_1 = 0.5Hz$ and $f_2 = 150Hz$ (for comparing later with the state-of-the-art) and then with $f_1 = 500Hz$ and $f_2 = 10KHz$ to englobe the ENG bandwidth, as follows:

$$V_{n_{RMS}} = \sqrt{\int_{f_1}^{f_2} V_n^2(f)df} \tag{3.2}$$

$$V_{n_{RMS}}^{150Hz} = 951.43nV$$

$$V_{n_{RMS}}^{10KHz} = 2.91\mu V$$

For the power, it was observed the overall contribution from the supply, in this case:

$$P = \overline{V_{DD} I_{total}} \tag{3.3}$$

$$P = 6.6\mu W$$

3.1.3 Common-mode input range & electrode offset rejection

Here it was checked at the input of the IA what was the common-mode input voltages (disconsidering the HPF, otherwise it would always be removed) that would still produce enough gain at the output. Essentially, it is changing the biasing point from the input transistors. For doing so, the input voltage was DC swept from GND to V_{DD} (0V to 1.2V). The result can be seen in Figure 3.6 and, therefore, the common-mode voltage must be in the range $0.2V \leq V_{CM} \leq 0.92V$ if the criteria is the 3dB gain loss.

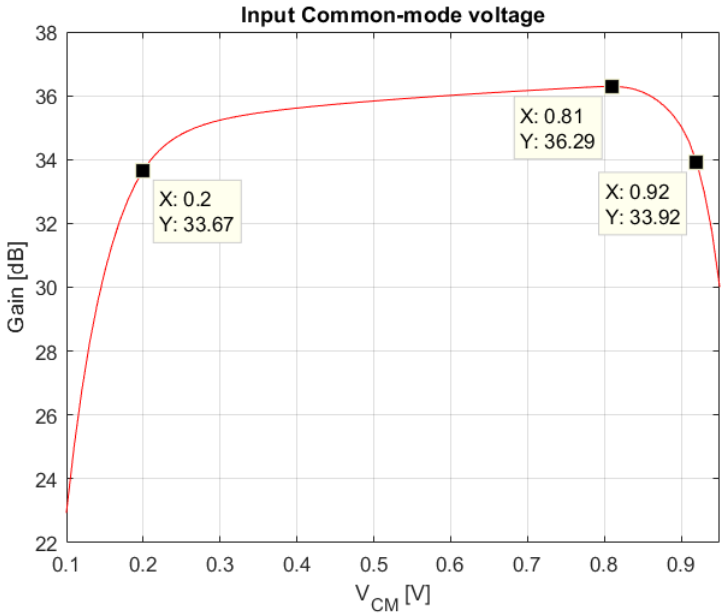

Figure 3.6: DC Common-mode input range

For the electrode offset rejection, it is needed to take into account the presence of the HPF at the input and, therefore, it is always removed. By using the HPF, however, the price to pay comes in the input impedance which is reduced.

3.1.4 Comparison with state-of-the-art

After highlighting some metrics from the IA, it can be seen in Table 3.2 the results. It can be clearly seen the power vs noise trade-off from the different papers. The majority of the IAs with higher CMRR than this current work presented some technique to improve the input impedance, such as boost impedance in [33]. After verifying the IA, now it is possible to build the true-tripolar amplifying architecture

including some additional features, as will be seen in the next section where it will be exploited the current mirror ratio from the IA to make it gain-tunable.

3.2 Digitally tunable gain CMIA

As seen in Tripolar amplifier configuarations section, the True-Tripolar configuration has the possibility to correct the impedance imbalance. However, this would only be possible if somehow the gains of the amplifiers were tunable. With this idea in mind and knowing the gain expression (3.1) from the IA in the previous section, by manipulating the current-mirror ratio a_{CM} it is possible to tune the gain to a certain value.

If the transistor MP6L in Figure 3.1b is replaced by a bank of transistors in parallel followed by digitally-controlled switches, then the gain can be tuned (see Figure 3.7). First, it is needed to define the range of imbalances to be corrected and also the accuracy desired. In other words, based on these values it will be possible to determine the full-scale of the gain and its resolution and, as such, the number of transistors in parallel as well as their sizes.

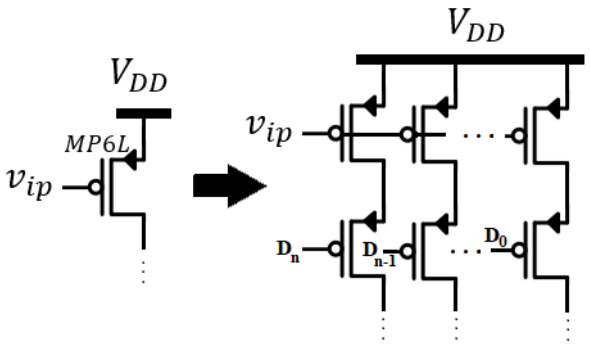

Figure 3.7: Replacing MP6L/R by a bank of transistors connected by switches

Specifications As suggested by [29] and [7], the target imbalances to be corrected will be up to $X_{imb} = \pm 40\%$. Following the result obtained in [7], the resolution will be done for ΔG chosen for when SIR > 6 dB.

Linking X_{imb} and SIR A relation from X_{imb} and SIR can be obtained by the equations below, where V_{TT} from (2.17) was renamed as V_{res} indicating the residual output from the EMG interference because of imbalances. Assuming ($G_{out} = 1$):

$$V_{res} = G_{out}\frac{Z_0 I_{INT}(G_2 Z_{t_2} - G_1 Z_{t_1})}{Z_0 + Z_t}$$
$$Z_{t_1} = \frac{Z_t(1 + X_{imb})}{2}$$
$$Z_{t_2} = \frac{Z_t(1 - X_{imb})}{2}$$
$$G_1 = G_2 = G$$

Grouping them all (3.4) it is obtained, moreover, the ENG output signal can be easily determined by (3.5):

$$V_{res} = I_{EMG} G \frac{X_{imb}}{\frac{1}{Z_t} + \frac{1}{Z_0}} \tag{3.4}$$
$$V_{ENG_{out}} = 2GV_{ENG} \tag{3.5}$$

Finally, using the SIR defined as the ratio between the signal $V_{ENG_{out}}$ and the interference V_{res}:

$$SIR = \frac{2V_{ENG}}{I_{EMG}\frac{X_{imb}}{\frac{1}{Z_t} + \frac{1}{Z_0}}} \tag{3.6}$$

Linking ΔG and X_{imb} Now, since there is a clear relation between SIR and imbalance, it is possible from a certain specification in SIR to determine the minimum imbalance allowed. The next step is to find a way to relate the gain with imbalance, to be able to link the specification to the desired gain. From ΔG perspective, defining the gains as follows and imposing null residual output it yields:

$$G_1 = G + \Delta G \tag{3.7}$$
$$G_2 = G - \Delta G \tag{3.8}$$
$$V_{TT} = 0 \tag{3.9}$$

Finally, using (3.7),(3.8) and (3.9) into (2.17):

$$\Delta G = -GX_{imb} \tag{3.10}$$

Full-scale and resolution for ΔG From (3.10), it is possible to determine the full-scale (FS) for ΔG and from (3.6) the resolution. Here it was decided for SIR > 6 dB following [7] result, as shown in Figure 3.8. From now on, the gain G will be 55.5 V/V, because as will be seen later, this value allows correction for ±40% imbalance range. By using that G = 55.5 V/V and the information from the graph, SIR = 6 dB leads to $X_{imb} = 0.54\%$, then, from (3.10):

$$\begin{aligned} |\Delta G_{step}| &= 55.5 * 0.54\% \quad [V/V] \\ |\Delta G_{step}| &= 0.3 \qquad [V/V] \end{aligned} \tag{3.11}$$

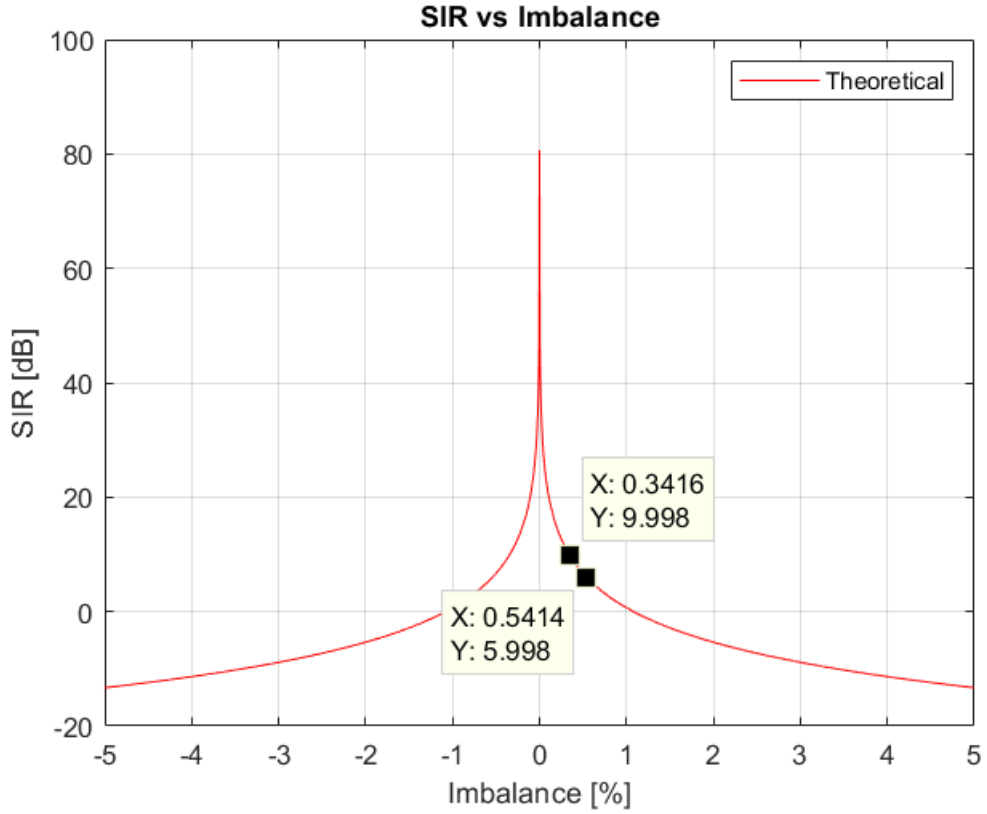

Figure 3.8: SIR in function of the imbalance

From (3.10), by using $X_{imb} = \pm 40\%$, it can be determined the maximum and minimum ΔG to correct the imbalances and, from that, the full-scale:

$$\begin{aligned} \Delta G_{min} &= -23 \quad [V/V] \\ \Delta G_{max} &= +23 \quad [V/V] \\ FS &= 46 \quad [V/V] \end{aligned} \tag{3.12}$$

Finally, from (3.12) and (3.11), the number of steps needed (N) are:

$$N = \frac{FS}{|\Delta G_{step}|} = \frac{46}{0.3}$$

$$N = 156.33 \tag{3.13}$$

As such, the minimum number of bits required for these steps is 8.

Recalculating ΔG_{LSB} and SIR For 8 bits the new gain step ΔG_{LSB}:

$$\Delta G_{LSB} = \frac{FS}{2^8}$$

$$\Delta G_{LSB} = 0.18 \quad [V/V] \tag{3.14}$$

From (3.14) and (3.10) the new imbalance is $X_{imb} = 0.32\%$, by looking at Figure (3.8), it can be seen that the new expected SIR is larger than 10 dB, in fact, expected $SIR > 10.4\ dB$. Now, the results can be summarized in Figure 3.9.

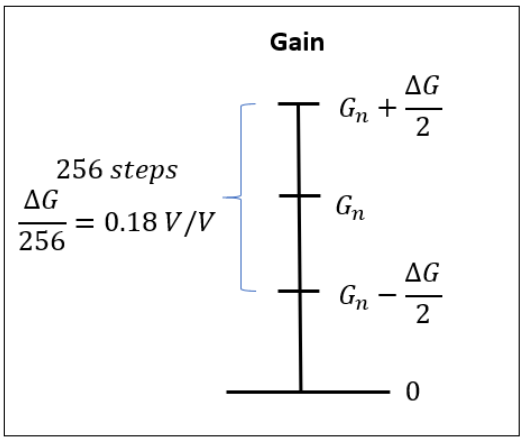

Figure 3.9: Nominal gain G_n and its increment ΔG relation

Linking ΔG_{LSB} with transistors size Finally, it is possible to define a size relationship from the nominal gain by using (3.1). Defining the aspect ratio as: $AR_i = \frac{W_i}{L_i}$, then:

$$G_n = \frac{R_2}{R_1}\frac{AR_n}{AR_2} \tag{3.15}$$

$$G_{LSB} = \frac{R_2}{R_1}\frac{AR_{LSB}}{AR_2} \tag{3.16}$$

By dividing (3.16) for (3.15) and isolating AR_{step}:

$$AR_{LSB} = \frac{G_{LSB}}{G_n} AR_n = \frac{0.18}{55.5} AR_n \tag{3.17}$$

$$\left(\frac{W}{L}\right)_{LSB} = 0.0032 \left(\frac{W}{L}\right)_n \tag{3.18}$$

With the relationship of equation (3.18) and Table 3.1, it is possible to determine the value required W_{LSB} and L_{LSB}. It is important to mention that because of simulation limitations, the minimum value allowed was $W_{LSB} = 200nm$, and the maximum length by the simulator was $L = 20\ \mu m$. As such, the minimum value allowed by ELDO was $\frac{W}{L} = 0.01$. For solving it, the technique used was to put transistors in series (in this case PMOS) connected by the same gate voltage. As such, these transistors in series are equivalent to one transistor but with larger length, as can be seen in Figure 3.10.

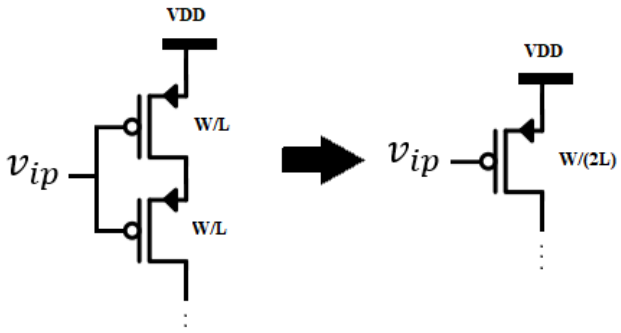

Figure 3.10: 2 identical transistors in series gate-connected equivalent to one with double length

Table 3.2: Comparison with the state-of-the-art from IAs

	This work	[33]	[8]	[34]	[9]	[35]	[5]
Technology	**65 nm**	0.18μm	0.8μm	0.5μm	65 nm	0.35μm	65 nm
Supply	**1.2 V**	1.2 V	1.8 V	3 V	1V	1V	0.6 V
Current	**5.5 μA**	13.3 μA	1.2μA	2.3 μA	1.8μA	385nA	28 nA
Gain	**39.8 dB**	28/26 dB	40 dB	n.a	40 dB	59/71 dB	51-96 dB
HPF corner	**0.5 Hz**	0.5 Hz	0.5 Hz	0.1 Hz	0.5 Hz	0.5 Hz	na
CMRR (@50/60Hz)	**> 75 dB**	> 110 dB	75 dB	120 dB	110 dB	83 dB	55 dB
Input Imp.	**177 MΩ**	> 500 MΩ	7.5 MΩ	>1GΩ	30 MΩ	NA	>100 MΩ
Input noise (range)	**2.91 μV_{RMS} (500Hz-10KHz)**	0.61 μV_{RMS} (150 Hz)	0.93 μV_{RMS} (100 Hz)	0.57 μV_{RMS} (25.6 KHz)	6.7 μV_{RMS} (100Hz)	1.15 μV_{RMS} (150 Hz)	6.52 μV_{RMS} (250Hz)

Chapter 4

Results

In this chapter it will be discussed the simulation results from the CMIA adding gain tunability, its validation and, finally, the results from the whole adaptive tripole digitally controlled compared to the state-of-the art.

4.1 Digitally tunable gain CMIA

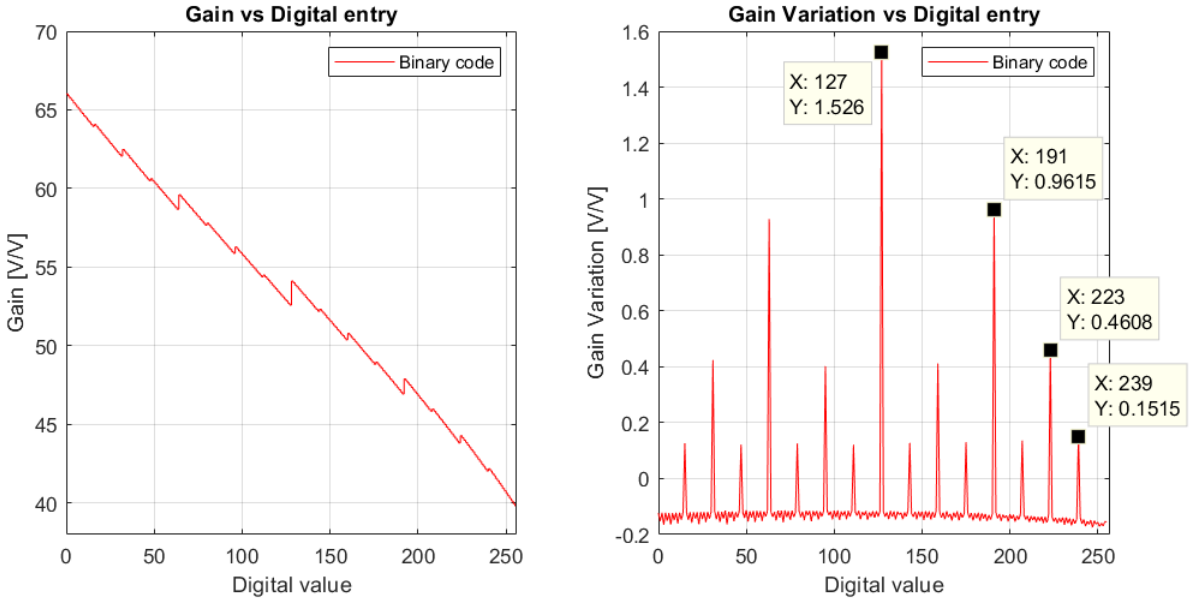

Figure 4.1: Gain and gain variations over digital entries

Binary-code The first idea was to use binary code for implementing the 8 bits from ΔG. As such, each transistor from the bank would have its $\frac{W}{L}$ increasing at

powers of 2 from the LSB to the MSB. The transistor responsible for the nominal gain G_n was kept always turned on with its initial sizes. The simulation for 8-bits in binary code can be seen in Figure 4.1.

As shown, the gain curve is not strictly decreasing, raising two main issues: 1) the imbalance range is not achieved, going against the specification previously decided; 2) in the paper [7], the correction from the gain is made through a feedback loop and, as consequence, with non-monotonicity, the gain compensation might end up unstable, because in the presence of imbalance the circuit should guide the gain to one direction, however, with this issue, the compensation might have the opposite effect.

In the second plot from Figure 4.1, it was highlighted the impact from the MSBs (it can be seen spikes at each 16, 32, 64 and 128 after the first one, at least). One way to address this problem is by using thermometer code, which is monotonic, however in order to obtain the same resolution the number of transistors would increase exponentially producing a control overhead. Another drawback is the area: despite of having the same active area, by replacing binary to thermometer, the transistors are splitted into smaller sizes but they must be slightly spaced demanding a larger overall area with the same happening for the switches.

In order to obtain the monotonicity characteristic from thermometer code and the high resolution from the binary one, it was decided to use a segmented code.

Segmented code The idea can be seen in Figure 4.2: the first bar representes the total width, the second the width division for binary code, the third for thermometer and, finally, the fourth, a mix of both codes. The second bar represents the 8-bits in binary, and they are binary controlled (0000 0001, 0000 0010,...). The problem of non-monotonicity from before happens, for example, when there is a mismatch between the MSB and all the other bits. From Figure 4.1, the largest gain variation happens for digital value 127, i.e, in the transition from 0111 1111 to 1000 0000. The third bar uses thermometer code where it keeps adding blocks (0000 0001, 0000 0011, 0000 0111,...) and, as such, it is monotonic. However, it reaches low resolution. The fourth bar represents a combination of both: 3 MSBs in thermometer code and 5 LSBs in binary code. As such, there are 7 control bits for the thermometer part and 5 control bits for the LSB. With such configuration there is less risk of non-monotonicity still preserving high resolution.

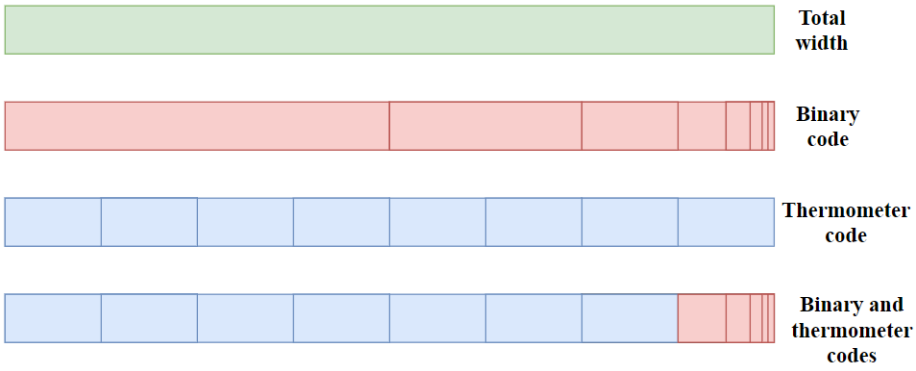

Figure 4.2: Segmented code: binary and thermometer codes together

The same idea can be extended for more MSBs and here it was done for 3 different cases: 1) 3 MSBs in thermometer + 5 LSBs in binary; 2) 4 MSBs in thermometer + 4 LSBs in binary; 3) 5 MSBs in thermometer + 3 LSBs in binary. The results and comparison with the binary code can be seen in Figure 4.3.

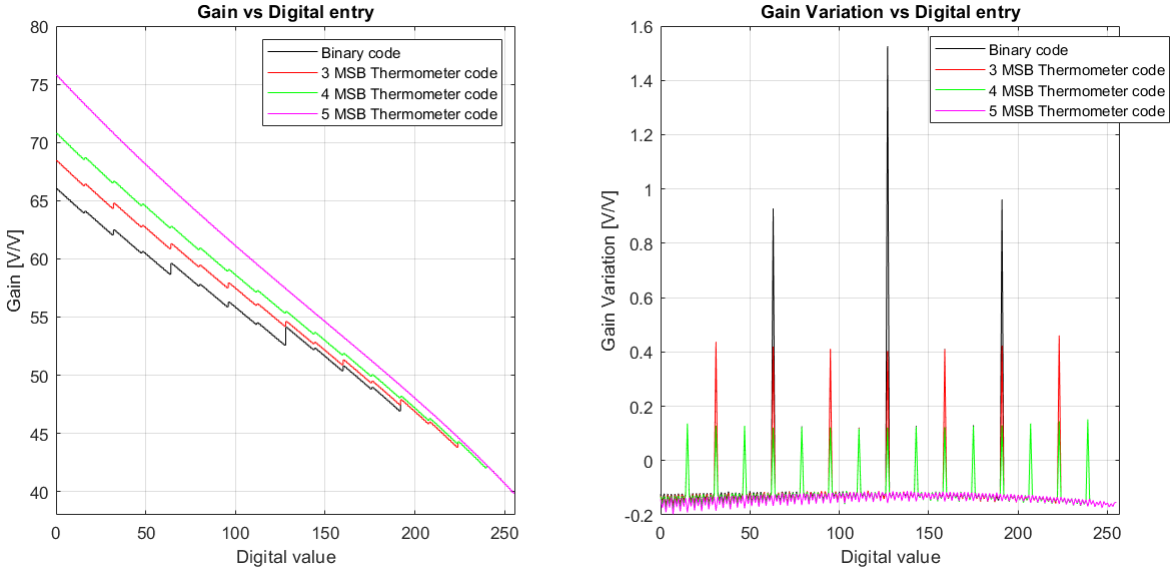

Figure 4.3: Comparison between segmented code for 3 cases and the binary one

From Figure 4.3 the more MSBs in thermometer, the more monotonic the curve is and the progression can be seen in the gain variation behaviour for each case. The configuration with 5 MSBs in thermometer + 3 LSBs in binary code was the only one to achieve monotonicity and, because of that, the chosen architecture. One remark about the graphs is that the nominal gain in use was different from the

ones that reached ±40% imbalance range correction, however, in this comparison the goal was to implement an architecture to ensure monotonicity and in all of them the same nominal gain was used. In the next simulations, the gain was corrected for the imbalance range and the transistor sizes can be seen in the Table 4.2, obtained by using (3.18). The suffix D0, D1, D2 corresponds to the 3 LSBs, while TH to thermometer transistors, where there are 31 in parallel but connected to switches with different control bits. NOM is the one responsible for the nominal gain.

Comparison with state-of-the-art After recalculating the parameters in the same way as did before, it can be made a comparison with the paper [6], that was the closest to the focus of this thesis. It can be seen, first, that the addition of the bank of transistors did not modify substantially the figures of merit from the IA, see Table 4.1. Unfortunately there are not many references available for comparison in a similar context. The gain from [6] varies by changing the tail current from an OTA and they reach very low noise at cost of high power, the opposite of this work, which has high noise but low power consumption.

Table 4.1: Comparison IA from this work (gain tunable) with [6]

	This work	[6]
Technology	**65 nm CMOS**	0.8 μm $CMOS$
Supply	**1.2 V**	±2.5 V
Power	**6.7 μW**	1.3 mW
Gain	**29 - 40 dB**	41 dB
Cut-off high	**10 KHz**	14 KHz
CMRR @1KHz	**84 dB**	82 dB
Input-referred noise (range)	**2.96 μV_{RMS} (500 Hz to 10 KHz)**	290 nV_{RMS} (1 Hz to 15 KHz)

Table 4.2: New MP6 transistors allowing the variable gain

Transistors	**(W/L)** $[\mu m/\mu m]$	**M**
MP6_D0	0.27/160	1
MP6_D1	0.27/80	1
MP6_D2	0.27/40	1
MP6_TH	0.27/20	31
MP6_NOM	0.83/10	3

4.2 Adaptive Tripole digitally-assisted

This architecture can be seen as such:

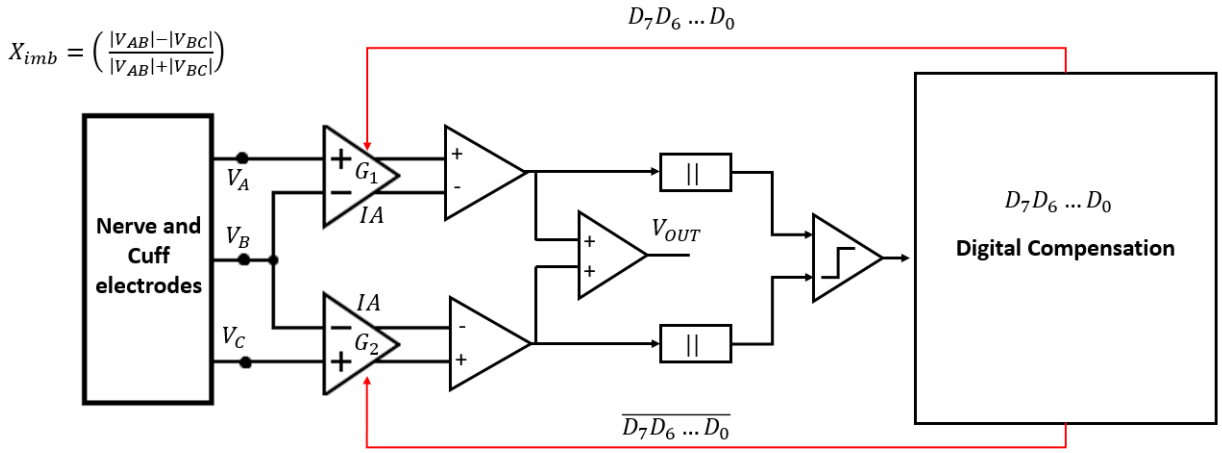

Figure 4.4: Adaptive tripole with digitally controlled gains

In this work, the main focus is in the gain tunability from the IA and ensuring its proper functioning. The blocks that are fed into the digital compensation, as shown in Figure 4.4, are some of the challenges for future works, not the focus here. In order to validate the circuit behaviour, a first simulation with no-imbalance and no-compensation was done. The result can be seen in Figure 4.5, for $V_{ENG} = 1\mu V$ and in the presence of the EMG signal.

After validating the gain tunability from the IA, the goal now is to make sure that the adaptive tripole corrects imbalances for the ±40% imbalance range. In Figure 4.6 it can be seen the SIR distribution for 0%, -40% and +40% imbalances. It shows that at least for the extremes the SIR observed is higher than 6 dB. The inputs were: $V_{ENG} = 1\mu V$ and $I_{EMG} = 1\mu A$ from the model seen in Figure 2.9. The other values used for the complete model can be seen in Table 2.2. The signal compensated and non-compensated for -40% can be seen in Figure 4.7.

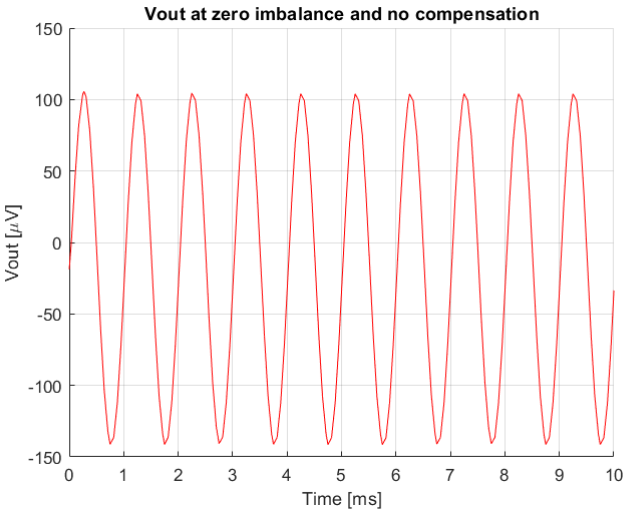

Figure 4.5: Output signal with no imbalance neither compensation

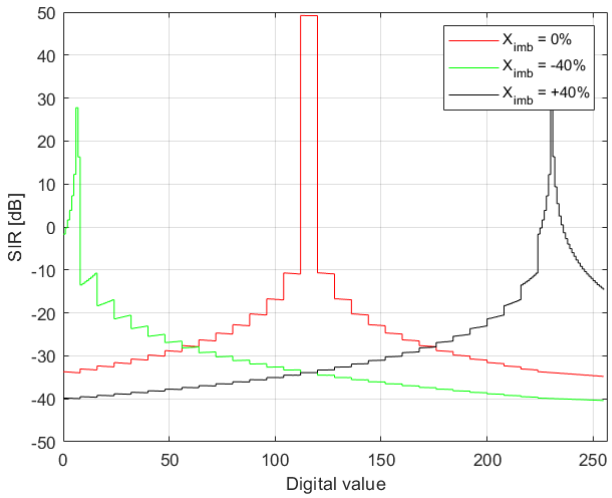

Figure 4.6: SIR distribution for $\pm 40\%$ and 0% imbalances

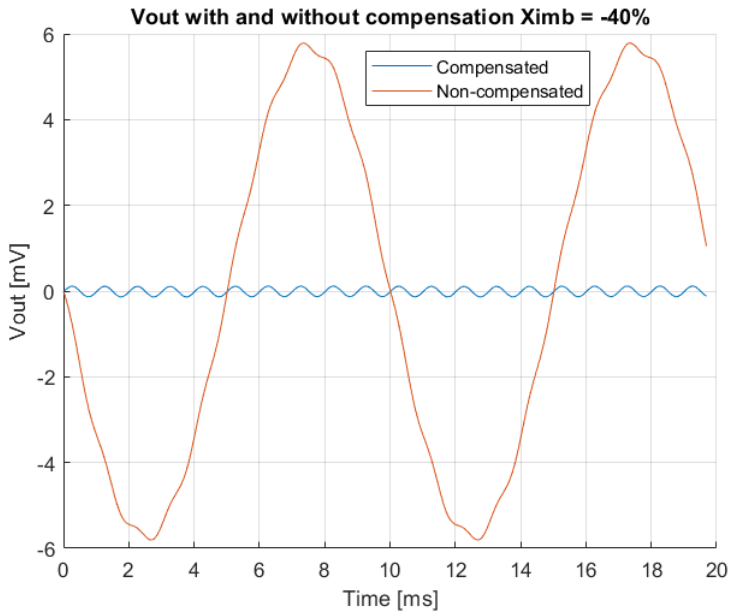

Figure 4.7: Signal compensated and non-compensated for Ximb = -40%

Taking a closer look at the compensated signal in Figure 4.8, the output value is coherent from what was expected, because its value should be $V_{out} = 2G_nV_{ENG} \approx 110\mu V_p$, due to the property from the true-tripole explored by adaptive-tripole (equation 2.18). Also notice that the result was the very close to the case with no-imbalance and no-compensation. One of the advantages from the way the implementation was made refers to the fact that whenever the compensation happens, the output ENG signal will always be close to $V_{out} = 2G_nV_{ENG}$, because from Figure 3.9 and (2.18), one IA will contribute with $G + \Delta G$ and the other with $G - \Delta G$, cancelling each other at the output after summation.

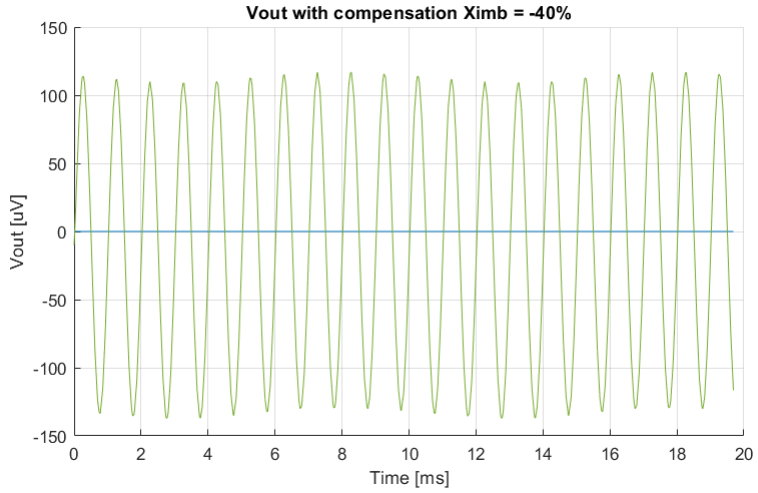

Figure 4.8: Signal compensated for Ximb = -40%, SIR = 27 dB

Finally, to show that the circuit works for the whole range, the simulation was run for all imbalances and picking the best SIR value for a specific digital entry. The result can be seen in Figure 4.9, where the minimum SIR was close to 10 dB and the largest around 50 dB.

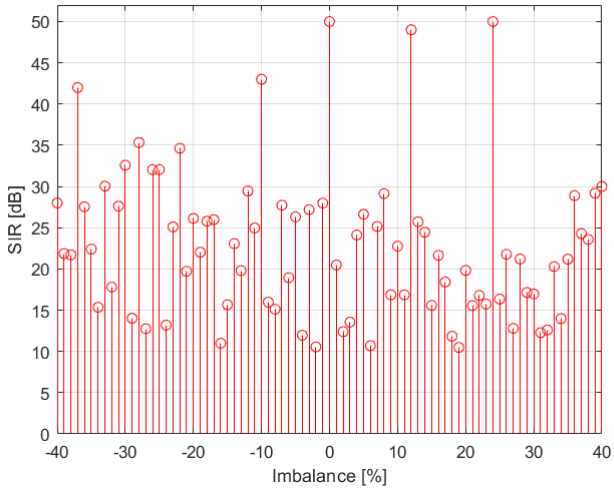

Figure 4.9: Largest SIR values for each imbalance

Comparison with state-of-the-art After gathering the performance metrics from the AT, they were compared with the state-of-the-art from the paper [7] and [6], as seen in Table 4.3. Unfortunately, there are not many references available

to do a broader comparison, however it is possible to observe some trade-offs. In both cited papers, it is used a low-noise pre-amplifier followed by a variable-gain OTA, allowing them to achieve very small noise values. Comparing the work in this thesis, it can be seen that the noise is quite detrimental for the sensing, since ENG signals have amplitudes close to few μV, the same order of magnitude from the input-referred noise, that would generate low SNR values. However, if this noise is somehow manageable by some technique, it would allow an implementation of a circuit more than 2 orders of magnitude less power consuming than the architectures from [7] and [6].

Table 4.3: Comparison adaptive-tripole with the state-of-the-art

	This work	[7]	[6]
Technology	**65 nm CMOS**	0.8 μm $BiCMOS$	0.8 μm $CMOS$
Supply	**1.2 V**	± 2.5 V	± 2.5 V
Power	**13.5 μW**	7.2 mW	3 mW
Gain	**36 - 44 dB**	$>$ 40 dB	$>$ 41 dB
Total ENG path gain	**41 dB**	87 dB	52.5 dB
Range of correction	**$\pm$40%**	$>$ 40 %	$\pm$5%
Gain resolution	**0.18 V/V**	Analog	Analog
Input-referred noise (range)	**3.14 μV_{RMS} (500 Hz to 10 KHz)**	291 nV_{RMS} (1 Hz to 15 KHz)	290 nV_{RMS} (1 Hz to 10 KHz)
SIR	**$>$ 10 dB**	$>$ 6 dB	$>$ -15.5 dB
THD	**$<$ 1.08%**	n.a	n.a

Chapter 5

Conclusion

In this part it will be given a summary with critical look to what was developed in this thesis, as well as some future work perspectives.

The main goal of this thesis was to be able to adapt the available IA from ECG applications to the ENG context, along with is integration in an amplifying architecture that dealt with the most proeminent non-idealities. From this perspective, reaching SIR $>$ 10 dB, with gain around 40 dB and low-power were some of the metrics that favor what was deployed. From the current-mirror ratio and its link with the gain, the opportunity to make a design that could benefit from it was clear after knowing how architectures such adaptive-tripole would exploit the gain tunability to deal with non-idealities. From the specifications and information from the state-of-the-art, the path and the methodology to be followed were decided and, as a result, the IA demanded 8 control bits in order to reach the full-range of imbalances to be corrected and the needed resolution. Determined the relation between the gain and the imbalances, linking them to the transistor sizes became trivial and the first obvious implementation came in binary code. Problems such non-monotonicity can make the circuit unstable if implemented in a feedback loop, as it is the main interest in the gain tunability. To overcome this issue commonly present in binary codes, a segmented control was used: a mix between thermometer code, that benefits from monotonicity, and binary that favors high resolution.

After validating the gain tunability, the next step was to implement the IA in the adaptive-tripolar configuration and testing it for different digital entries to compensate imbalances. After verified expected behaviour from the circuit, it was possible to compare all the work with some other references in the literature, such as [7] and [6]. From that, some major considerations must be made. The first one is the noise, where the thermal level gets predominant and when input-referred reaches the same order of magnitudes from the desired ENG signals (while they reach one order of magnitude less noise). Another point is that the use of a high-pass filter to remove DC electrode offsets reduces the input impedance, that

contributes for not reaching as large CMRR [32],[17] as other architectures. When designing a circuit for ENG purposes, if the idea is to long-term implantation, then low-noise architectures as in this work should be considered, despite of the high noise content. Some techniques used for improving SNR could be used, for example, with multi-channel sensing, where the signal could be collected as different realizations from the same phenomena, by averaging the SNR would increase as a factor $\sqrt{N}$, where N is the number of repetitions from the same event [12]. Even with low SNR, with data post-processing, by using FFT it is also possible to detect the peaks and extract some information.

Future work Some parts of the circuit presented in Figure 4.4 are still missing, for example, for the decision making in order to allow the AT system to be autonomous. Following the same idea as in [7], with a rectifier followed by an comparator it would be possible to determine to which direction compensate the imbalances in the AT. Insisting in the same architecture from this work, it would be interesting to find a method to deal with the noise in a clever way without substantial power overhead.

Bibliography

[1] Clinical methods: The history, physical, and laboratory examinations, 1990.

[2] AERJournal. Deep brain stimulation.

[3] L. N. S. Andreasen and J. J. Struijk. Signal strength versus cuff length in nerve cuff electrode recordings. *IEEE Transactions on Biomedical Engineering*, 49(9):1045–1050, 2002.

[4] L. N. S. Andreasen, J. J. Struijk, and M. Haugland. An artificial nerve fiber for evaluation of nerve cuff electrodes. In *Proceedings of the 19th Annual International Conference of the IEEE Engineering in Medicine and Biology Society. 'Magnificent Milestones and Emerging Opportunities in Medical Engineering' (Cat. No.97CH36136)*, volume 5, pages 1997–1999 vol.5, 1997.

[5] Y. Chen, D. Jeon, Y. Lee, Y. Kim, Z. Foo, I. Lee, N. B. Langhals, G. Kruger, H. Oral, O. Berenfeld, Z. Zhang, D. Blaauw, and D. Sylvester. An injectable 64 nw ecg mixed-signal soc in 65 nm for arrhythmia monitoring. *IEEE Journal of Solid-State Circuits*, 50(1):375–390, 2015.

[6] A. Demosthenous, J. Taylor, I. F. Triantis, R. Rieger, and N. Donaldson. Design of an adaptive interference reduction system for nerve-cuff electrode recording. *IEEE Transactions on Circuits and Systems I: Regular Papers*, 51(4):629–639, 2004.

[7] A. Demosthenous and I. F. Triantis. An adaptive eng amplifier for tripolar cuff electrodes. *IEEE Journal of Solid-State Circuits*, 40(2):412–421, 2005.

[8] T. Denison, K. Consoer, A. Kelly, A. Hachenburg, and W. Santa. A 2.2/spl mu/w 94nv//spl radic/hz, chopper-stabilized instrumentation amplifier for eeg detection in chronic implants. In *2007 IEEE International Solid-State Circuits Conference. Digest of Technical Papers*, pages 162–594, 2007.

[9] Q. Fan, F. Sebastiano, J. H. Huijsing, and K. A. A. Makinwa. A 1.8 μ w 60 nv/$\sqrt{}$ hz capacitively-coupled chopper instrumentation amplifier in 65

nm cmos for wireless sensor nodes. *IEEE Journal of Solid-State Circuits*, 46(7):1534–1543, 2011.

[10] Kirsten Fiest, Khara Sauro, Samuel Wiebe, Scott Patten, Churl-Su Kwon, Jonathan Dykeman, Tamara Pringsheim, Diane Lorenzetti, and Nathalie Jette. Prevalence and incidence of epilepsy: A systematic review and meta-analysis of international studies. *Neurology*, 88:10.1212/WNL.0000000000003509, 12 2016.

[11] Franz Fürbass. *EEG monitoring based on automatic detection of seizures and repetitive discharges*. PhD thesis, 12 2017.

[12] Umer Hassan and Sabieh Anwar. Reducing noise by repetition: Introduction to signal averaging. *European Journal of Physics*, 31:453, 03 2010.

[13] Nick Van Helleputte. Short course sensor interfaces for internet of everything. pages 1–97, 12 2016.

[14] Bernhard Hiebl, Bog S, Ralf Mikut, Bauer C, Ole Gemeinhardt, Friedrich Jung, and Krüger T. In vivo assessment of tissue compatibility and functionality of a polyimide cuff electrode for recording afferent peripheral nerve signals. *Applied Cardiopulmonary Pathophysiology*, 14, 01 2010.

[15] Jin Li, Sio Pun, Mang Vai, Pengun Mak, Pui-In Mak, and Feng Wan. Design of current mode instrumentation amplifier for portable biosignal acquisition system. pages 9 – 12, 12 2009.

[16] Jaakko Malmivuo and Robert Plonsey. *Bioelectromagnetism. 13. Electroencephalography*, pages 247–264. 01 1995.

[17] Coen Metting van Rijn, Abraham Peper, and Cornelis Grimbergen. High quality recording of bioelectric events. part 1. interference reduction, theory and practice. *Medical biological engineering computing*, 28:389–97, 10 1990.

[18] NHS. Overview epilepsy.

[19] World Health Organization. Epilepsy.

[20] C. Pflaum, R. R. Riso, and G. Wiesspeiner. Performance of alternative amplifier configurations for tripolar nerve cuff recorded eng. In *Proceedings of 18th Annual International Conference of the IEEE Engineering in Medicine and Biology Society*, volume 1, pages 375–376 vol.1, 1996.

[21] R. Rieger, J. Taylor, A. Demosthenous, N. Donaldson, and P. J. Langlois. Design of a low-noise preamplifier for nerve cuff electrode recording. *IEEE Journal of Solid-State Circuits*, 38(8):1373–1379, 2003.

[22] Francisco Rodriguez, Dolores Ceballos, Martin Schuettler, Antoni Valero, Elena Valderrama, Thomas Stieglitz, and Xavier Navarro. Polyimide cuff electrodes for peripheral nerve stimulation. *Journal of neuroscience methods*, 98:105–18, 07 2000.

[23] Moacyr Rosa and Sarah Lisanby. Somatic treatments for mood disorders. *Neuropsychopharmacology : official publication of the American College of Neuropsychopharmacology*, 37:102–16, 01 2012.

[24] R. B. Stein, D. Charles, T. Gordon, J. Hoffer, and J. Jhamandas. Impedance properties of metal electrodes for chronic recording from mammalian nerves. *IEEE Transactions on Biomedical Engineering*, BME-25(6):532–537, 1978.

[25] J. J. Struijk and M. Thomsen. Tripolar nerve cuff recording: stimulus artifact, emg and the recorded nerve signal. In *Proceedings of 17th International Conference of the Engineering in Medicine and Biology Society*, volume 2, pages 1105–1106 vol.2, 1995.

[26] J. J. Struijk, M. Thomsen, J. O. Larsen, and T. Sinkjaer. Cuff electrodes for long-term recording of natural sensory information. *IEEE Engineering in Medicine and Biology Magazine*, 18(3):91–98, 1999.

[27] Johannes Struijk and M. Thomsen. Tripolar nerve cuff recording: stimulus artifact, emg and the recorded nerve signal. volume 2, pages 1105 – 1106 vol.2, 10 1995.

[28] Lars Stumpp, Hugo Smets, Simone Vespa, Joaquin Cury, Pascal Doguet, Jean Delbeke, Emmanuel Hermans, Cristian Sevcencu, Thomas Nielsen, Antoine Nonclerq, and Riëm El Tahry. Recording of spontaneous vagus nerve activity during pentylenetetrazol-induced seizures in rats. *Journal of Neuroscience Methods*, 343:108832, 06 2020.

[29] I. F. Triantis, A. Demosthenous, and N. Donaldson. On cuff imbalance and tripolar eng amplifier configurations. *IEEE Transactions on Biomedical Engineering*, 52(2):314–320, 2005.

[30] Iasonas Triantis. *An adaptive amplifier for cuff imbalance correction and interference reduction in nerve signal recording.* PhD thesis, 06 2005.

[31] Epilepsy Society UK. What is epilepsy.

[32] N. Van Helleputte, S. Kim, H. Kim, J. P. Kim, C. Van Hoof, and R. F. Yazicioglu. A 160 μa biopotential acquisition ic with fully integrated ia and motion artifact suppression. *IEEE Transactions on Biomedical Circuits and Systems*, 6(6):552–561, 2012.

[33] N. Van Helleputte, M. Konijnenburg, J. Pettine, D. Jee, H. Kim, A. Morgado, R. Van Wegberg, T. Torfs, R. Mohan, A. Breeschoten, H. de Groot, C. Van Hoof, and R. F. Yazicioglu. A 345 μw multi-sensor biomedical soc with bio-impedance, 3-channel ecg, motion artifact reduction, and integrated dsp. *IEEE Journal of Solid-State Circuits*, 50(1):230–244, 2015.

[34] R. F. Yazicioglu, P. Merken, R. Puers, and C. Van Hoof. A 200 μ w eight-channel eeg acquisition asic for ambulatory eeg systems. *IEEE Journal of Solid-State Circuits*, 43(12):3025–3038, 2008.

[35] X. Zou, W. Liew, L. Yao, and Y. Lian. A 1v 22μw 32-channel implantable eeg recording ic. In *2010 IEEE International Solid-State Circuits Conference - (ISSCC)*, pages 126–127, 2010.

UNIVERSITÉ CATHOLIQUE DE LOUVAIN
École polytechnique de Louvain
Rue Archimède, 1 bte L6.11.01, 1348 Louvain-la-Neuve, Belgique | **www.uclouvain.be/epl**